

# Canonical-Polyadic-Decomposition of the Potential Energy Surface Fitted by Warm-Started Support Vector Regression

Zekai Miao,<sup>1,2</sup> Xingyu Zhang,<sup>1</sup> Qingfei Song,<sup>1</sup> and Qingyong Meng<sup>1, a)</sup>

<sup>1)</sup>*Department of Chemistry, Northwestern Polytechnical University, West Youyi Road 127, 710072 Xi'an, China*

<sup>2)</sup>*Department of Computer Science and Technology, University of Cambridge, 15 JJ Thomson Avenue, CB3 0FD Cambridge, United Kingdom*

(Dated: 1 November 2024)

**Abstract:** In this work, we propose a decoupled support vector regression (SVR) approach for direct canonical polyadic decomposition (CPD) of a potential energy surface (PES) through a set of discrete training energy data. This approach, denoted by CPD-SVR, is able to directly construct the PES in CPD with a more compressed form than previously developed Gaussian process regression (GPR) for CPD, denoted by CPD-GPR (*J. Phys. Chem. Lett.* **13** (2022), 11128). Similar to CPD-GPR, the present CPD-SVR method requires the multi-dimension kernel function in a product of a series of one-dimensional functions. We shall show that, only a small set of support vectors play a role in SVR prediction making CPD-SVR predict lower-rank CPD than CPD-GPR. To save computational cost in determining support vectors, we propose a warm-started (ws) algorithm where a pre-existed crude PES is employed to classify the training data. With the warm-started algorithm, the present CPD-SVR approach is extended to the CPD-ws-SVR approach. Then, we test CPD-ws-SVR and compare it with CPD-GPR through constructions and applications of the PESs of  $H + H_2$ ,  $H_2 + H_2$ , and  $H_2/Cu(111)$ . To this end, the training data are computed by existed PESs. Calculations on  $H + H_2$  predict a good agreement of dynamics results among various CPD forms, which are constructed through different approaches.

**Keywords:** *Potential Energy Surface; Canonical Polyadic Decomposition; Support Vector Regression; Quantum Dynamics; Low Rank*

---

<sup>a)</sup>Electronic mail: qingyong.meng@nwpu.edu.cn

## I. INTRODUCTION

In propagating nuclear wave function with the grid-based representation<sup>1,2</sup>, the whole configurational space is represented by a given set of grids. In this context, an  $f$ -dimension potential energy surface (PES) as a continuous function of coordinates,  $V(q^{(1)}, \dots, q^{(f)})$ , has to be (approximately) represented in a tensor form  $V(q_{i_1}^{(1)}, \dots, q_{i_f}^{(f)}) = V_{i_1, \dots, i_f} = V_I$ , where  $\{q^{(\kappa)}\}_{\kappa=1}^f$  is the set of  $f$  coordinates and  $I = \{i_\kappa\}_{\kappa=1}^f$  denotes a set of tensor indices. Moreover, in modern approaches to propagate nuclear wave function, such as multi-configurational time-dependent Hartree (MCTDH) method<sup>3-5</sup> and its multi-layer version (ML-MCTDH)<sup>6-8</sup>, the nuclear wave function must be expanded as a series of products of few-particle functions. In Heidelberg version of MCTDH and ML-MCTDH<sup>3-5,8</sup>, the potential tensor  $V_I$  has to be accordingly transferred to a sum-of-products (SOP) form<sup>9-16</sup> or canonical polyadic decomposition (CPD) form<sup>17-19</sup>. The latter is a special class of SOP. In this work, since the SOP and CPD forms play the above important role in wave function propagations, we propose a new approach to build the PES in the CPD form through support vector regression (SVR). It was developed as one of data-driven techniques with sparse kernel function space and was recently suggested<sup>20</sup> as a possible approach in building the PES in general form.

Usually, the potential function in the SOP/CPD form is constructed using an existing analytical PES through an appropriate algorithm leading to a two-step scheme (see counterclockwise steps in Figure 1). First, the analytical PES is constructed through a database. Second, the PES in the SOP/CPD form is re-fitted. In 1990s, Meyer and co-workers<sup>9-11</sup> proposed the POTFIT (means potential re-fitting) algorithm to construct the SOP form on grids whose total amount must be less than  $2 \times 10^9$ . For high-dimension models, the multi-grid POTFIT (MGPF)<sup>12,13</sup>, multi-layer POTFIT (MLPF)<sup>14,15</sup>, Monte-Carlo POTFIT (MCPF)<sup>16</sup> algorithms have been designed and implemented. Schröder<sup>17</sup> found that the PES in the CPD form is effective for high-dimension propagation. Employing the Monte Carlo approach, the MCCPD algorithm<sup>17</sup> was proposed to construct the CPD form. Later, the MCCPD method in conjugation with 21-dimension (21D) ML-MCTDH calculations were launched<sup>18</sup> proving the power of MCCPD as well as the CPD form. Recently, a 75D PES of the hydrogen atom scattering off non-rigid graphene surface<sup>19</sup> was re-fitted in the CPD form by MCCPD further showing its power. Although the above algorithms for the two-step scheme were proved to be powerful<sup>9-18</sup> in re-fitting the PES in either the SOP/CPD form, direct construction of SOP or CPD potential function through discrete energy data must be developed leading to a one-step scheme. As shown by clockwise step of Figure 1, the one-step

scheme avoids constructing the PES in general form and thus saves computational cost because constructions of both general form and SOP/CPD form are very expensive. In 2006, Manzhos and Carrington Jr.<sup>21</sup> used exponential activation function to construct a neural-network (NN) function to represent potential functions in the CPD form. In 2014, Koch and Zhang<sup>22</sup> found another kind of single-layer NN function for constructing the CPD potential and proposed the SOP-NN method. In addition, Peláez and co-workers<sup>23,24</sup> proposed a SOP or CPD form of finite basis representation (FBR), denoted by SOP-FBR or CP-FBR. By both of them, a guess of initial SOP/CPD functional form is optimized to yield either SOP or CPD form through existing potential function.

In 2022, a direct construction of the CPD form, called CPD-GPR<sup>25</sup>, was proposed on the basis of Gaussian process regression (GPR)<sup>20,26</sup>. Recently, combining several coordinates with strong couplings into one logical coordinate, the mode-combination (mc) version of CPD-GPR was proposed<sup>27</sup>, denoted by CPD-mc-GPR. Employing CPD-mc-GPR, a 9D PES of OH + HO<sub>2</sub> was directly constructed in mode-combined CPD form<sup>27</sup>. This construction under the one-step scheme opening a new door to build the PES of realistic reaction in CPD tensor form. However, both CPD-GPR and CPD-mc-GPR produce number of decomposition terms, called rank of CPD, is equal to number of the training energy data<sup>25,27</sup>. Comparing with MCCPD<sup>17</sup> that gives the CPD rank of  $10^2 \sim 10^3$ , a typical rank of  $10^3 \sim 10^4$  provided by CPD-mc-GPR largely reduces the efficiency of subsequent quantum dynamics calculation<sup>27</sup>. To overcome this problem, in this work noting its sparse kernel feature, the SVR method is further developed leading to a new implementation of the one-step scheme, called CPD-SVR. Because prediction of SVR depends on the number of support vectors which is usually smaller than that of training data<sup>20</sup>, the present CPD-SVR method is able to produce the CPD form with smaller rank. Furthermore, SVR consumes lots of computational cost in determining support vectors, a warm-started (ws) algorithm is proposed in this work to improve efficiency leading to CPD-ws-SVR. Essentially, the present CPD-ws-SVR is a kernel regression with a kernel function in product form, while a selection algorithm for choosing support vectors is employed to accelerate convergence. In this work, we test the present CPD-ws-SVR method and compare it with CPD-GPR by building the PES of H + H<sub>2</sub>. The CPD form is also constructed by the POTFIT and MCCPD methods to show the power of CPD-ws-SVR by performing MCTDH calculations.

The rest of this paper is organized as follows. In Section II, we shall describe the theoretical framework of CPD-ws-SVR. Section III presents details of test calculations. Finally, Section IV concludes with a summary.

## II. THEORETICAL FRAMEWORK

### A. The CPD-SVR Method

First of all, we have to briefly describe concept of the CPD form. For an  $f$ -dimensional potential function  $V(q^{(1)}, \dots, q^{(f)})$ , its CPD form on a set of grids  $I = \{i_\kappa\}_{\kappa=1}^f$  is given by<sup>17,18,25</sup>

$$V(q_{i_1}^{(1)}, \dots, q_{i_f}^{(f)}) \simeq V^{(\text{CPD})}(q_{i_1}^{(1)}, \dots, q_{i_f}^{(f)}) = V_I^{(\text{CPD})} = \sum_r^R c_r \prod_\kappa^f v_{r,i_\kappa}^{(\kappa)} = \sum_r^R c_r \Omega_{r,I}, \quad (1)$$

where  $R$  is the expansion order, that is the CPD rank, while the product  $\Omega_{r,I} = \prod_\kappa^f v_{r,i_\kappa}^{(\kappa)}$  is introduced for clarity. The normalized functions  $v_r^{(\kappa)}(q_{i_\kappa}^{(\kappa)})$  are called the single-particle potentials (SPP), exclusively depend on only one variable. Here, we denote that  $v_{r,i_\kappa}^{(\kappa)} = v_r^{(\kappa)}(q_{i_\kappa}^{(\kappa)})$  for the  $i_\kappa$ -th grid of the  $\kappa$ -th degree of freedom (DOF). Having  $V_I^{(\text{CPD})}$  in Equation (1), the remaining task is to find both the expansion functions  $\Omega_{r,I}$  and the coefficients  $c_r$ . This motivates the present developments of CPD-SVR and its warm-started version (CPD-ws-SVR).

Before giving CPD-SVR and CPD-ws-SVR, a brief description of SVR is necessary. We shall return to the warm-started SVR (ws-SVR) later. To construct the  $f$ -dimensional PES, a total of  $n$  energy points  $\{\mathbf{X}, \mathbf{E}\} = \{\mathbf{X}_j, E_j\}_{j=1}^n$ , must be computed in advance by *ab initio*. Matrices  $\mathbf{X}$  and  $\mathbf{E}$  are  $f \times n$  coordinate matrix and  $n \times 1$  energy matrix, respectively. Then, a regression model that reproduces the energy at  $f \times 1$  coordinate vector  $\mathbf{x}$ , denoted by  $y(\mathbf{x})$ , is optimized through  $\{\mathbf{X}, \mathbf{E}\}$ . In general, the SVR prediction function<sup>20</sup>,

$$y(\mathbf{x}) = \phi^T \cdot \bar{\omega} + b = \mathbf{K}_*^T \cdot \bar{\varphi} + b, \quad (2)$$

depends on a set of support vectors which are the data points most difficult to regress and have direct bearing on the optimum location of the target PES, as illustrated by Figure 2. Therefore, the support vector lies on and outside the two hypersurfaces that are parallel to the target prediction  $y(\mathbf{x})$  with the distance of given tolerance error  $\pm\epsilon$ . In Equation (2),  $\bar{\omega}$  and  $\bar{\varphi}$  are optimized parameter matrices and  $\mathbf{K}_*^T = \phi^T \Phi$  is  $1 \times p$  kernel-function matrix, where  $\phi$  and  $\Phi$  are feature space of  $\mathbf{x}$  and  $\mathbf{X}$ , respectively, while  $p$  is dimensionality of the feature space<sup>20</sup>. We refer the reader to Reference<sup>20</sup> for numerical details on SVR.

Similar to CPD-GPR<sup>25</sup>, according to Equation (2), the SVR potential function  $V^{(\text{SVR})}(\mathbf{x}) = y(\mathbf{x})$  can be expanded as

$$V_I^{(\text{SVR})} = V^{(\text{SVR})}(\mathbf{x}_I) = V_{i_1, \dots, i_f}^{(\text{SVR})} = \sum_{r=1}^{n_{\text{sv}}} \bar{\varphi}_r K(\mathbf{x}_I, \mathbf{X}_r) + b, \quad (3)$$

where  $K(\mathbf{x}_I, \mathbf{X}_r)$  and  $\bar{\varphi}_r$  are the  $r$ -th elements of the  $\mathbf{K}_*^T$  and  $\bar{\varphi}$  matrices, respectively, which  $\mathbf{x}_I$  is coordinate matrix with elements  $\{q_{i_k}^{(\kappa)}\}_{\kappa=1}^f$ . We further assume that the multi-dimension kernel function  $K(\cdot, \cdot)$  is given in a product form of  $\{K^{(\kappa)}(\cdot, \cdot)\}_{\kappa=1}^f$  that depend on only one variable,

$$K(\mathbf{x}, \mathbf{X}_r) = \prod_{\kappa=1}^f K^{(\kappa)}(q^{(\kappa)}, Q_r^{(\kappa)}), \quad (4)$$

where  $Q_r^{(\kappa)}$  is the  $\kappa$ -th element of the coordinate matrix  $\mathbf{X}_r$ . Here, we would like to remind that  $\mathbf{X}_r$  is the  $r$ -th coordinates set of the training data and thus it is already known. Substituting Equation (4) into Equation (3), we finally obtain the CPD-SVR potential values on grids,

$$V_I^{(\text{CPD-SVR})} = \sum_{r=1}^{n_{\text{sv}}} \bar{\varphi}_r K(\mathbf{x}_I, \mathbf{X}_r) + b = \sum_{r=1}^{n_{\text{sv}}} \bar{\varphi}_r \prod_{\kappa=1}^f K^{(\kappa)}(q_{i_k}^{(\kappa)}, Q_r^{(\kappa)}) + b = \sum_{r=1}^{n_{\text{sv}}} \bar{\varphi}_r \prod_{\kappa=1}^f K_{r,i_k}^{(\kappa)} + b, \quad (5)$$

where  $K_{r,i_k}^{(\kappa)} = K^{(\kappa)}(q_{i_k}^{(\kappa)}, Q_r^{(\kappa)})$  means value of the kernel function for the  $\kappa$ -th DOF on the  $i_k$ -th grid. Comparing Equation (5) with Equation (1), the potential tensor  $V_I^{(\text{CPD-SVR})}$  already has the CPD form. Only restriction for such expression is the assumption of Equation (4). Using the denotation in Equation (5), the kernel function in this work for the  $\kappa$ -th DOF is given by

$$K^{(\kappa)}(q^{(\kappa)}, Q_r^{(\kappa)}) = \exp\left(-\frac{(q^{(\kappa)} - Q_r^{(\kappa)})^2}{2l^2}\right), \quad (6)$$

where  $l$  is hyper-parameter. As already expected, since  $n_{\text{sv}} < n$  the CPD rank by CPD-SVR is smaller than that by CPD-GPR. The present CPD-SVR approach is thus able to obtain lower-rank CPD form.

At the first glance, the present CPD-SVR approach is somewhat trivial from the viewpoint of mathematics due to the simple revisions on potential model and the kernel function. Comparing CPD-GPR<sup>25</sup>, the present CPD-SVR approach employs sparser inner-product space as shown by Equation (5). However, noting that SVR is just a mathematical tool in fitting the PES, it must be further revised and implemented to make it possible in application scenario. This means that a special algorithm has to be designed to implement our own goal, that is the CPD construction with low rank. We would like to emphasize that improvements on the PES construction might not have only a single goal but also be applicable to subsequent quantum dynamics calculations. The present goal does not only focus on the fitting error but also does focus on reducing the CPD rank. Furthermore, the SVR method consumes lots of computational cost in selecting the support vectors because of the sequential minimal optimization (SMO) algorithm<sup>20</sup>. Therefore, let us turn to the warm-started algorithm for accelerating the present CPD-SVR approach.

## B. Warm-Started SVR Algorithm

The SVR calculation requires that the training energy data are added into the optimization procedure in batches or one-by-one and hence consumes lots of computational time. To overcome this problem, a warm-started SVR scheme, denoted by ws-SVR, is proposed in this work. This approach needs an existing potential function  $U(\mathbf{x})$  which might be crudely constructed by either regression or interpolation through the some training database that will be used in either ws-SVR or CPD-ws-SVR calculations. Moreover, function  $U(\mathbf{x})$  must be cheap but should correctly predict the PES topology. We define difference function between the ws-SVR potential and the crude potential in the form

$$F(\mathbf{x}) = \mathbf{K}_*^T \cdot \boldsymbol{\varphi} + b + U(\mathbf{x}). \quad (7)$$

With function  $F(\mathbf{x})$  of Equation (7), two rounds of optimization should be launched. The first round of optimization with  $m$  training data requires the error function for the  $i$ -th training energy

$$h(\mathbf{X}_i) = F(\mathbf{X}_i) - E_i = \sum_{j=1}^m \varphi_j K_{ij} + b + U(\mathbf{X}_i) - E_i, \quad i = 1, 2, \dots, m, \quad (8)$$

where  $K_{ij} = K(\mathbf{X}_i, \mathbf{X}_j)$ . Turning to  $m$  training data, one may sample these data by an appropriate and chemistry-informed distribution in the configurational space making the resulting error as small as possible. However, the present purpose is reduction of the CPD rank by SVR, instead of sampling of these initial data. For simple, the present  $m$  training data are randomly distributed to show the implementation of SVR. Next, setting tolerance error  $\epsilon > 0$ , the  $i$ -th training point  $\{\mathbf{X}_i, E_i\}$  must belong to one of the following three sets. First, if  $h(\mathbf{X}_i) \in (-\epsilon, +\epsilon)$  then  $\{\mathbf{X}_i, E_i\}$  belongs to remain set  $\mathcal{R}$  where corresponding coefficient  $\varphi_i$  is equal to zero. Second, if  $h(\mathbf{X}_i) = \pm\epsilon$  then  $\{\mathbf{X}_i, E_i\}$  belongs to support set  $\mathcal{S}$  with  $\varphi_i \in (-c, +c)$ . Finally, if  $h(\mathbf{X}_i) \in (-\infty, -\epsilon) \cup (+\epsilon, +\infty)$  then  $\{\mathbf{X}_i, E_i\}$  belongs to error set  $\mathcal{E}$  with  $\varphi_i = \pm c$ . Here,  $c$  is a given hyper-parameter of the regression model. With the above definitions, one can determine classifications of a total of  $m$  training points after this round of optimization.

Now, the second round of optimization could be performed by adding one new point  $\{\mathbf{X}_\ell, E_\ell\}$  in the training database and then new classifications of these  $m + 1$  training points have to be determined. After the second round of optimization, it is easy to find that  $F(\mathbf{X}_i)$  becomes

$$F(\mathbf{X}_i) = \sum_{j=1}^m \varphi'_j K_{ij} + \varphi_\ell K_{i\ell} + b' + U(\mathbf{X}_i), \quad (9)$$

and hence the error function becomes

$$h(\mathbf{X}_i) = \sum_{j=1}^m \varphi'_j K_{ij} + \varphi_\ell K_{i\ell} + b' + U(\mathbf{X}_i) - E_i. \quad (10)$$

The apostrophe indicates that the corresponding parameter is updated due to a second round of optimization. Comparing Equation (10) with Equation (8) the difference between two optimizations by adding the  $\ell$ -th training point is given by

$$\Delta h(\mathbf{X}_i) = \sum_{j=1}^m (\varphi'_j - \varphi_j) K_{ij} + \varphi_\ell K_{i\ell} + (b' - b). \quad (11)$$

By Equation (11), if the KKT condition is met and all of training points always belong to the original set, only those in  $\mathcal{S}$  are changed making  $h(\mathbf{X}_k) = \pm\epsilon$  a constant and  $\Delta h(\mathbf{X}_k) = 0$ , implying the expression

$$\sum_{s \in \mathcal{S}} (\varphi'_s - \varphi_s) K_{is} + \varphi_\ell K_{i\ell} + (b' - b) = \sum_{s \in \mathcal{S}} \Delta \varphi_s K_{is} + \varphi_\ell K_{i\ell} + \Delta b = 0. \quad (12)$$

By Equation (12), it is possible to determine new classification for the  $i$ -th training point  $\{\mathbf{X}_i, E_i\}$  leading to the working equations of wa-SVR. Derivations by Equations (11) and (12) are given in the Supporting Information file. We only give a brief description of the working equations themselves.

### C. Selecting Process of Support Vectors

By the KKT condition, we have  $\sum_{i=1}^m \varphi_i = 0$  and hence  $\sum_{i=1}^m (\varphi'_i - \varphi_i) + \varphi_\ell = 0$ . Since only the training point in  $\mathcal{S}$  is able to change the coefficients, in Supporting Information we prove that

$$\sum_{s \in \mathcal{S}} (\varphi'_s - \varphi_s) + \varphi_\ell = 0, \quad (13)$$

$$\begin{pmatrix} \Delta b \\ \Delta \varphi_{s_1} \\ \dots \\ \Delta \varphi_{s_m} \end{pmatrix} = - \begin{pmatrix} 0 & 1 & \dots & 1 \\ 1 & K_{s_1 s_1} & \dots & K_{s_1 s_m} \\ \dots & \dots & \dots & \dots \\ 1 & K_{s_m s_1} & \dots & K_{s_m s_m} \end{pmatrix}^{-1} \begin{pmatrix} 1 \\ K_{s_1 \ell} \\ \dots \\ K_{s_m \ell} \end{pmatrix} \varphi_\ell = \boldsymbol{\lambda} \varphi_\ell, \quad (14)$$

where  $\{s_i\}_{i=1}^m$  is set of indices for the training points in  $\mathcal{S}$ ,  $\boldsymbol{\lambda}$  a  $(m+1) \times 1$  matrix with  $\lambda_j$  as elements. By Equation (14), it is possible to update  $\boldsymbol{\varphi}$  and  $b$  leading to its name of updating equation. Now, let us show how to update function  $h(\mathbf{X}_i)$ . Since the error function of support vectors are always

equal to  $\pm\epsilon$ , only the training data in  $\mathcal{R}$  or  $\mathcal{E}$  change the error function. Thus, by indices  $\{e_i\}_{i=1}^m$  for data in  $\mathcal{R}$  or  $\mathcal{E}$ , Equation (11) can be rewritten in the matrix form

$$\begin{pmatrix} 0 \\ \Delta h(\mathbf{X}_{e_1}) \\ \dots \\ \Delta h(\mathbf{X}_{e_m}) \end{pmatrix} = \begin{pmatrix} 1 \\ K_{e_1\ell} \\ \dots \\ K_{e_m\ell} \end{pmatrix} + \begin{pmatrix} 0 & 1 & \dots & 1 \\ 1 & K_{e_1s_1} & \dots & K_{e_1s_m} \\ \dots & \dots & \dots & \dots \\ 1 & K_{e_ms_1} & \dots & K_{e_ms_m} \end{pmatrix} \boldsymbol{\lambda} \cdot \varphi_\ell = \boldsymbol{\gamma} \cdot \varphi_\ell, \quad (15)$$

where  $\boldsymbol{\gamma}$  is a  $(m+1) \times 1$  matrix with  $\gamma_j$  as elements. By resolving Equation (15) one can update the error function  $h(\mathbf{X}_i)$ . Equations (14) and (15) are thus working equations of the present ws-SVR approach.

Now, We should explore the updating scheme of the classifications of the training data and show the role of existed potential function  $U(\mathbf{x})$ . We graphically collect updating scheme of the training data in Figure 3 and briefly describe cases of this scheme in Table I. In general, two cases for adding new data exist in implementing ws-SVR. In Case #1, the new point (denoted by index  $\ell$ ) is added into  $\mathcal{R}$  implying that  $|h(\mathbf{X}_\ell)| < \epsilon$  (see the upper panel of Figure 3) and the other points are unchanged. In Case #2, the new point is added into  $\mathcal{E}$  or  $\mathcal{S}$  making the decision surface of the last round changed and the last classifications might be changed. However, in order to minimize changes in one optimization round, we should keep the training data belonging to their original sets as much as possible. This is because the updating scheme by Equations (14) and (15) requires a prerequisite that every training data will not leave their original set implying that the classification of the training points must be fixed. This is, of course, not the case when a new round of optimization is finished. Careful analysis easily indicates four different situations in changing the classification during optimization, as given in the lower panel of Figure 3.

In the first situation, the  $i$ -th training point is moved from  $\mathcal{E}$  to  $\mathcal{S}$ . Since function  $h(\mathbf{X}_i)$  is changed from  $h(\mathbf{X}_i) \in (-\infty, -\epsilon) \cup (+\epsilon, +\infty)$  to  $h(\mathbf{X}_i) = \pm\epsilon$ , *i.e.*  $\Delta h(\mathbf{X}_{e_i}) = \pm\epsilon - h(\mathbf{X}_{e_i})$ , Equation (15) implies  $\Delta\varphi_\ell = \boldsymbol{\gamma}_{e_i}^{-1}(\pm\epsilon - h(\mathbf{X}_{e_i}))$ . The second situation is that the  $i$ -th point is moved from  $\mathcal{R}$  to  $\mathcal{S}$  and thus difference of the error function is  $\Delta h(\mathbf{X}_{r_i}) = \pm\epsilon - h(\mathbf{X}_{r_i})$ , where  $\{r_i\}_{i=1}^m$  represent set of indices of the training point in  $\mathcal{R}$ . By updating equation (that is Equation (14)), one can have  $\Delta\varphi_\ell = \boldsymbol{\gamma}_{r_i}^{-1}(\pm\epsilon - h(\mathbf{X}_{r_i}))$ . In the third situation, the  $i$ -th point is moved from  $\mathcal{S}$  to  $\mathcal{R}$ . One can similarly have got  $\Delta\varphi_\ell = \boldsymbol{\lambda}_{s_i}^{-1}\varphi_{s_i}$ . In the fourth situation the  $i$ -th point is moved from  $\mathcal{S}$  to  $\mathcal{E}$  implying that  $\Delta\varphi_\ell = \boldsymbol{\lambda}_{s_i}^{-1}(\pm\epsilon - \varphi_{s_i})$ . All of the above cases are collected in Table I. These cases imply that the pre-existed potential function  $U(\mathbf{x})$  is helpful in updating classifications of the training points and accelerating the SVR calculations. Due to this ability of function  $U(\mathbf{x})$ , the SVR calculations



become to be warm-started leading to the name of ws-SVR. Combination ws-SVR and CPD-SVR, we finally obtain the CPD-ws-SVR approach. Having the CPD-ws-SVR method, we should inspect its power in the PES construction. Collected in Table II are three examples for testing the CPD-ws-SVR approach, in particular for testing the ws-SVR implementation. In Table II, we also give numerical details of the present SVR calculations. These examples are H + H<sub>2</sub>, H<sub>2</sub> + H<sub>2</sub>, and H<sub>2</sub>/Cu(111).

### III. RESULTS AND DISCUSSIONS

#### A. Calculations on H + H<sub>2</sub>

The first benchmark is the quantum dynamics of the H + H<sub>2</sub> reaction which is typical and simple for testing the PES. The Jacobi coordinates set is used to define the positions of three atoms, as given in Table II. To define this system, the center-of-mass (COM) of the H<sub>2</sub> molecule is denoted by G. The Jacobi coordinates set for H + H<sub>2</sub> contains bond length  $r_v$  of H<sub>2</sub>, dissociation length  $r_d$  between the impacting H atom and G, and their included angle  $\theta$ . With the Jacobi coordinates, the Hamiltonian operator is given by<sup>28</sup>

$$\hat{H}_{H_3} = -\frac{1}{2M} \frac{\partial^2}{\partial r_d^2} - \frac{1}{2\mu} \frac{\partial^2}{\partial r_v^2} - \left( \frac{1}{2Mr_d^2} + \frac{1}{2\mu r_v^2} \right) \left( \frac{1}{\sin \theta} \frac{\partial}{\partial \theta} \sin \theta \frac{\partial}{\partial \theta} \right) + V_{H_3}(r_d, r_v, \theta), \quad (16)$$

where  $M$  and  $m$  are reduced masses along  $r_d$  and  $r_v$ , respectively. In Equation (16), the PES term  $V_{H_3}(r_d, r_v, \theta)$  in CPD form are constructed through the present CPD-ws-SVR approach on the basis of the training data prepared by pre-existed BKMP2 PES, where the potential energy of thoroughly separated three H atoms is set to be zero. Unless otherwise specified, the atomic units are used in this paper. Based on the Hamiltonian operator given by Equation (16), quantum dynamics calculations are performed using the Heidelberg MCTDH package<sup>29</sup>. We refer the reader to References<sup>3-5</sup> for details of MCTDH. In the present MCTDH calculations, the vibration ground state of the H<sub>2</sub> molecule is used as reactants, while the third H atom is located at  $r_d^{(0)} = 4.5$  bohr with an initial momentum of 8.0 au moving towards H<sub>2</sub>. Here, the ranges of coordinates are  $1.00 \leq r_d \leq 9.04$ ,  $0.60 \leq r_v \leq 6.24$ , and  $0 \leq \theta \leq \pi/2$ , while 68, 48, and 31 grid points are used, respectively. To ensure convergence in MCTDH calculations, the single-particle function (SPF) size of  $r_d/r_v/\theta = 20/20/20$  is used. Numerical details of the present dynamics calculations are collected in Table III.

Turning to CPD-ws-SVR, the one-dimensional kernel functions for all DOFs have the same form, as given by Equation (6). To test the resulting PES, the validation data are randomly selected in the whole configuration space. The fitting errors of the CPD-ws-SVR calculations are illustrated in Figure 4 as function of number of training data  $n$ . These errors clearly indicate the convergence of the size of database. For instance, setting  $\epsilon = 10^{-4}$  hartree the present CPD-ws-SVR calculations predict convergence at  $n > 7000$  where the root mean squared error (RMSE) approaches to  $2 \times 10^{-3}$  hartree (*i.e.*,  $< 54$  meV). Moreover, as illustrated in Figure 4, the convergence curves for RMSE as function of  $n$  weakly depend on the tolerance error  $\epsilon$ . This feature is clear for the blue and black curves of Figure 4 where  $\epsilon$  is  $10^{-3}$  and  $10^{-4}$  hartree. Generally, the smaller the tolerance error is, the smaller the RMSE value should be but the larger the computational cost should be. This implies the dependence of the convergence curves on  $\epsilon$ . As previously discussed<sup>20</sup>, however, since no noise exists in the training database, if the tolerance error is small enough the fitting RMSE depends on  $\epsilon$  weakly, or even independent on  $\epsilon$ . This can be understood with the aid of Figure 2(a). The support vectors lie on and outside the two hypersurfaces that are parallel to the target prediction function with distances of tolerance error  $\pm\epsilon$ . The optimal potential function stems from the function class with the biggest capacity of independent samples that one can twiddle keeping the functional form not too complex. If no noise exists in the training database, the support vectors should independent on the choice of  $\epsilon$ . This point is clear by comparing the solid lines with dashed lines in Figure 2(b). Therefore, cost-performance of SVR might become lower when  $\epsilon$  is too small.

Furthermore, Figure 5 illustrates distributions of support vectors associated with the potential energy, including distributions of  $n_{sv}/n$  and  $n_{sv}$ . It is clear that the ratio  $n_{sv}/n$  approaches to roughly 80% at lower-lying energy region, while such ratio slowly approaches to about 60% at middle-lying energy region and then quickly decreases to about 30% at higher-lying energy region. Because of Equation (5), comparing with the CPD-GPR approach<sup>25</sup>, the CPD rank computed by CPD-ws-SVR is reduced by a factor of  $\sim 70\%$  making the expansion expression of Equation (5) more contracted than that of CPD-GPR. The fact that the ratio  $n_{sv}/n$  is a decreasing function of potential energy, as given by Figure 5, might be caused by different importance of different energy regions. Since the lower-lying region plays much more important role in chemistry dynamics than the middle- and higher-lying regions, more attention must be paid on lower-lying region in regression. In lower-lying energy regions which contain reactants, products, transition state, and probable intermediate, the reaction occurs along these steady points. In other region with higher-

lying potential energy, the potential function is either flat if distances among atoms are very large or steeply increases if one or some of these distances are very small. Because of existences of the steady points, the first- or second-order derivatives in lower-lying energy regions usually vary more significantly than those in higher-lying energy regions, say those with large distances among the atoms. Since the lower-lying energy regions contain all of steady points along the reaction coordinate and hence all of information in the reaction, the learning processes for lower-lying energy regions are more complex than those for higher-lying energy regions. Such region is hence difficult to build making the ratio  $n_{sv}/n$  larger than that of other region.

Finally, illustrated in Figure 6 gives two-dimension contour cut together with three-dimension surface of the present CPD-ws-SVR PES at  $\theta = \pi/2$  where  $n = 9000$  and  $\epsilon = 10^{-4}$  hartree while the number of support vectors is determined to be  $n_{sv} = 5726$ . By Figure 6 one can clearly find that the topology of the present PES with RMSE of  $< 1.8 \times 10^{-3}$  hartree (*i.e.*  $< 50$  meV) is satisfactory because this RMSE value approaches to the chemical accuracy ( $\sim 43$  meV). Optimizing the distribution of the training data and hyper-parameters of the SVR model<sup>20</sup>, the CPD-ws-SVR calculations indicate the RMSE of  $\sim 10^{-4}$  hartree ( $\sim 2.7$  meV) which is within the results by standard tools. To further test the present CPD-ws-SVR calculations, extensive MCTDH calculations are performed on the PESs that have been constructed through various methods. Illustrated in Figure 7 are present reactive probability curves comparing with previously reported curves<sup>25</sup>. To compute these curves, the PESs in CPD or SOP were constructed through POTFIT, MCCPD, and CPD-GPR, while the PES constructed by SVR is shown by Figure 6. As shown in Figure 7, a good agreement among these reactive probabilities can be found when the total energy is smaller than  $-2.0$  eV. This clearly implies accuracy of the present CPD-ws-SVR calculations, even though the distribution of training data and hyper-parameters of SVR are not optimized.

## B. Calculations on $\text{H}_2 + \text{H}_2$ and $\text{H}_2/\text{Cu}(111)$

Having considered the  $\text{H} + \text{H}_2$  system in Section III A, we turn to the testing calculations for the  $\text{H}_2 + \text{H}_2$  and  $\text{H}_2/\text{Cu}(111)$  systems whose coordinates are given in Table II. To construct their PESs, the training data are computed through existing PESs<sup>30-32</sup> instead of *ab initio* energy calculations because the main purpose of the present calculations is to show the power of CPD-ws-SVR. For each system, we randomly sample the training data and validate data forming training set and validate set, respectively, composing of a total of  $5 \times 10^5$  energy data. Then, 6D CPD-GPR and

CPD-ws-SVR calculations are performed to build new PESs in the CPD form. With the errors on validate sets as functions of the number of training data  $n$ , one can discuss the convergence of regressions and compare CPD-ws-SVR with CPD-GPR. Moreover, to show the power of SVR in reducing the CPD rank, the number of support vectors  $n_{sv}$  together with ratios of number of support vector to training data  $n_{sv}/n$  are given as functions of the number of training data. In the present CPD-ws-SVR calculations, the tolerance error is set to be  $10^{-4}$  hartree that is used for the case of  $H + H_2$ .

Before giving numerical results of the present CPD-ws-SVR and CPD-GPR calculations, we would like to mention that, quantum dynamics of the  $H_2 + H_2$  and  $H_2/Cu(111)$  systems based on the PESs fitted in this work require multi-dimension MCTDH calculations. In technique, direct MCTDH calculations by such PESs are still difficult, because such multi-dimension MCTDH calculations need the mode combination (mc) scheme, where two or three coordinates are combined into one logical coordinate<sup>5</sup>. Recently, the CPD-GPR approach has been further implemented by us using the mode-combination scheme leading to the CPD-mc-GPR approach<sup>27</sup>. A 9D test for  $OH + HO_2$  indicates that CPD-mc-GPR has capability to build the CPD potential in the mode-combination scheme to promote efficiency in multi-dimension ML-MCTDH calculations<sup>27</sup>. Further testing high-dimensional CPD-mc-GPR calculations is also planned. Similarly, to reduce the rank of the CPD-mc-GPR potential, the SVR technique should be adopted leading to CPD-mc-ws-SVR approach for multi-dimension MCTDH calculations. Since many difficulties and challenges exist in implementing CPD-mc-ws-SVR, it is planned in the future work on multi-dimension ML-MCTDH calculations on  $OH + HO_2 \rightarrow O_2 + H_2O$ . As will be shown in this work (see below), the SVR technique has power to reduced the CPD rank. We believe that further multi-dimension ML-MCTDH calculations must be possible, even though theoretical challenges still exist as will be discussed in Section III C below.

Illustrated in Figure 8 are convergence inspections of the present CPD-GPR and CPD-ws-SVR calculations for testing systems. By Figure 8, we can easily conclude the following two points. First, varying the number of training data the GPR calculations are more fast approach convergence than the SVR calculations. As shown by Figure 8(a), the 3D CPD-GPR calculations for  $H + H_2$  approach to convergence if  $n \geq 5 \times 10^3$ , while the 6D ones approach to convergence if  $n \geq 1.5 \times 10^4$ . As shown by Figure 4, however, the 3D CPD-ws-SVR calculations approach to convergence when  $n \geq 8 \times 10^3$ . Of course, convergence depends on the tolerance error as well, as shown by Figure 4. Meanwhile, as shown by Figure 8(b), the 6D CPD-ws-SVR calculations approach to convergence

when  $n \geq 5 \times 10^4$ . Second, for each system, the validate error of CPD-GPR is generally smaller than that of CPD-ws-SVR. For  $\text{H} + \text{H}_2$ , the validate error of GPR is almost zero (see also the green line of Figure 8(a)), but that of CPD-ws-SVR is about  $10^{-3}$  hartree (see also Figure 4). Comparing Figure 8(a) with Figure 8(b), the validate errors of 6D CPD-GPR are almost twice those of 6D CPD-ws-SVR. We shall interpret these numerical results on convergence, in particular the error performance of the present CPD-ws-SVR calculations in Section III C below.

Next, let us turn to the number of support vectors  $n_{\text{sv}}$  as function of the training data  $n$ . Unlike the black dots of Figure 5, given in Figure 9 are ratios of the number of support vectors to that of training data as function of  $n$ , that is ratio  $n_{\text{sv}}/n$  as function of  $n$ . As usual, the blue and red lines represent results of the  $\text{H}_2 + \text{H}_2$  and  $\text{H}_2/\text{Cu}(111)$  systems, respectively. When  $n \leq 10^4$ ,  $n_{\text{sv}}/n$  for  $\text{H}_2 + \text{H}_2$  and  $\text{H}_2/\text{Cu}(111)$  are both identical to roughly 0.7 implying reduction of the CPD rank. When  $n$  increases, however, the situation becomes interesting. For the  $\text{H}_2 + \text{H}_2$  system (see the blue line of Figure 9), the  $n_{\text{sv}}/n$  curve mutates from 0.7 to about 0.88 at  $n \sim 10^4$ . Further increasing  $n$ , the  $n_{\text{sv}}/n$  curve decreases slowly from 0.88 to roughly 0.82 at  $n \sim 10^5$ . Turning to the  $\text{H}_2/\text{Cu}(111)$  system, as shown by the red line of Figure 9, there exists mutation at  $n \sim 10^5$ . Moreover, these two curves are approximately parallel to each other at the interval of  $10^4 < n < 10^5$  while they seem to become identical at  $n > 10^5$ . The reason why there are such features is still not clear at the present. Exploring the thermodynamic nature of the data in building the PES is planning.

### C. Discussions on Numerical Results

The convergence inspections illustrated in Figures 4 and 8 indicate that the CPD-ws-SVR calculations predict the resulting potential function with larger validate error than the CPD-GPR calculations. Now, we are arriving at the position to compare 6D CPD-ws-SVR for  $\text{H}_2 + \text{H}_2$  and  $\text{H}_2/\text{Cu}(111)$  with 3D case for  $\text{H} + \text{H}_2$  and then to interpret the reasons why the present 6D CPD-ws-SVR calculations produce rather poor performance than that for  $\text{H} + \text{H}_2$ . First, it should be mentioned that the present CPD-ws-SVR calculations are performed to show the present implementation and thus the computational setups in the SVR calculations have not yet optimized. According to our previous discussions<sup>20</sup>, it is still difficult to optimize a part of hyper-parameters (see Equations (22) and (29) of Reference<sup>20</sup>) in optimizing the SVR target. Since optimization algorithm of the SVR hyper-parameters is missed, these hyper-parameters are chosen by experiences and several tests. Due to such insufficient optimizations, the present SVR performance is

rather poor in fitting error. Second, as illustrated by Figure 4, the tolerance error influences the validate error of the resulting SVR potential function. Answer of the question how to determine the tolerance error is still missed. As have discussed in Section III A, for the training set without any noise, the smaller the tolerance error is, the smaller the training error is, even though a large amount of computational costs might be consumed. But, the situation changes for the training set with noise. In this case, if the tolerance error is set to be too small SVR may predict larger validate error (see also Figure 2). Therefore, implementation of SVR must be much more carefully designed to approach small enough validate error. Third, optimization targets of GPR and SVR are different<sup>20</sup> making the present 6D CPD-ws-SVR calculations for  $\text{H}_2 + \text{H}_2$  and  $\text{H}_2/\text{Cu}(111)$  perform rather poor than CPD-GPR. As previously discussed<sup>20</sup>, the GPR approach optimizes likelihood while the SVR approach, or more precisely support vector machine (SVM), is a decision process instead of an optimization process. Although the decision process is essentially a kind of optimization too, the target in SVR is to select the support vectors among the training data. Thus, one has to carefully perform the SVR calculations for the targets to minimize fitting error. Finally, in selecting process of SVR, the present CPD-ws-SVR method requires an existing function  $U(\mathbf{x})$  to help this process, as shown by Figure 3. Because the existing function  $U(\mathbf{x})$  is roughly constructed and imprecise, this  $U(\mathbf{x})$ -aided selecting process should be iterative to optimize number and distribution of the support vectors. Balancing the computational cost in SVR and fitting error, one must stop the iterative process if it approaches some criterion.

In general, fitting error depends on various factors in practical PES construction, such as quality and distribution of the training database<sup>33-37</sup>. The construction approach, instead of a functional model itself, may be a factor in producing the fitting error. However, methodology is even not the most important factor. As previously discussed<sup>20</sup>, almost all of modern construction approaches can be merged in a unified regression model, implying that different approaches should produce similar fitting error. On the one hand, quality of the training data generally represent the noises of the data. The *ab initio* energy calculations often produce noises depending on the regions in the configuration space. If the noises are too large, the PES construction might predict rather large error<sup>26,28</sup>. The segmented strategy<sup>26,38</sup> was thus proposed to reduce the noises improving the construction quality, where the potential functions of a small region are constructed. On the other hand, distribution of the training data might be the most important factor in fitting the PES. If the data sampled in the regions with fruitful chemistry-information, relationships among these data are useful to reproduce dynamics and easily learned by the PES model leading to small errors.

In the present work, the training data are computed by existed PESs which are continuous and smooth functions implying the training data without any noise. However, these data are randomly distributed in the whole configuration space making most of chemistry informations be watered down. This random distribution products a rather high fitting error if no further optimization has been made. Improivng this distribution and sampling the training data along the reaction coordinate, the present CPD-ws-SVR approach is able to produce the fitting errors of  $10^{-4} \sim 10^{-5}$  hartree (namely  $10^0 \sim 10^1$  meV), which is similar to or smaller than that from popular fitting approaches (say NN). Very recently, a general scheme for sampling the data was proposed by us<sup>27,39</sup> where a unsupervised data-driven technique is adopted. Tests of this new sampling scheme was also reported<sup>39</sup>. Furthermore, due to the complex relationships among the training data, the functional form must be flexible enough to well converge the regression process implying a large amount of (hyper-)parameters that need to be optimized. The more flexible the potential function is, the more training data are needed consuming a large amount of computational cost. Therefore, special algorithms should be developed to reduce computational cost.

Next, turning to Figure 1 let us discuss the present one-step scheme on directly constructing the CPD potential function and show its advantages by comparing CPD-SVR/GPR with the MCCPD method<sup>17-19</sup>. First, although MCCPD is powerful in re-fitting the PES in CPD for high-dimension system, such as either 21D model of CO/Cu(100)<sup>18</sup> or 75D model of H/graphene<sup>19</sup>, a force-field-type potential has been employed for the MCCPD calculations<sup>17-19</sup>. This is because the MCCPD approach requires a large amount of Monte Carlo trajectories to approach convergence in integrating<sup>17-19</sup> and high-performance potential is much more appropriate. In other words, either NN or GPR PES is low-performance to implement the MCCPD calculations. This is not surprising because high-dimension NN and GPR function is generally very complex functional form with a large number of (hyper-)parameters leading to lower-performance. To overcome this problem, as the second point, we propose the one-step scheme as shown in Figure 1. In the two-step scheme (the anticlockwise one), one has to improve the numerical performance of the NN or GPR PES making it possible to implement for MCCPD. However, functional flexibility and numerical performance form a contradiction making the one-step scheme might impossible for high-dimension systems. In this context, the two-step scheme (the clockwise one) may be an appropriate choice. It is the present construction scheme for the CPD potential. By CPD-GPR/SVR the contradiction between functional flexibility and numerical performance is totally removed. As a general rule of thumb, in fitting a PES one should first consider its application scenario and thus one has to

carefully design the construction processes. Therefore, under the grid-based representation one might want to choose the two-step scheme of Figure 1 in fitting the PES for quantum dynamics calculations. Despite the above advantages, dependence of the CPD rank by the one-step scheme,  $n$  or  $n_{sv}$ , and the question how to further reduce the CPD rank are still open questions. One has to overcome this disadvantage to extend the applications of the one-step scheme.

#### D. Discussions on Similar Methods

Now, other methods to construct the PES in SOP/CPD should be discussed. Part of discussions have been simply given in Reference<sup>25</sup>. The first point is relationship among SOP-NN, CPD-GPR, and CPD-SVR which belong to the one-step scheme. The SOP-NN approach<sup>21,22</sup> uses a single-layer NN function to achieve a similar degree of complexity and non-linearity as multi-layer NN in the SOP form. The SOP-NN potential values on grids  $I$  are given by<sup>21,22</sup>

$$V_I^{(\text{SOP-NN})} = b_1^{(2)} + \sum_{m=1}^{\eta} w_{1m}^{(2)} \prod_{\kappa=1}^f F^{(\kappa)}(b_{m\kappa}^{(1)} + w_{m\kappa}^{(1)} q_{i_\kappa}^{(\kappa)}), \quad (17)$$

where  $\{b_{m\kappa}^{(1)}, b_1^{(2)}\}$  is biases set and  $\{w_{m\kappa}^{(1)}, w_{1m}^{(2)}\}$  is weights set while  $\eta$  is the number of neurons. Function  $F^{(\kappa)}(\cdot)$  is one-dimension activation function. Obviously, the SOP-NN approach actually produces the PES in the CPD form and hence it can be denoted by CPD-NN instead of SOP-NN. Product of all one-dimension activation functions is hence the activation function of the whole NN function. Noting that the kernel function of CPD-GPR has the same product characteristic of one-dimension functions, this might indicate hidden equivalence between SOP-NN and CPD-GPR. As previously discussed<sup>20</sup>, this is not surprising because the single-layer NN function is essentially equivalent to the GPR prediction. Moreover, the SVR approach can be considered to lie between the generalized linear regression (GLR), say NN, and kernel model for regression (KMR), say GPR. The present CPD-SVR approach can be considered to lie between SOP-NN and CPD-GPR and has some of their common features. For instance, number of support vectors  $n_{sv}$  is smaller than that of training data  $n$  and approximately equal to that of neurons  $\eta$ . Moreover, SVR requires kernel function instead of activation function making SVR similar to a kind of KMR.

Second, let us pay more attention on relationship between SOP-NN and CPD-SVR. As given by Equations (5) and (17) rank of  $V_I^{(\text{SOP-NN})}$  is number of neurons  $\eta$  while that of  $V_I^{(\text{CPD-SVR})}$  is number of support vectors  $n_{sv}$ . We have shown the argument of  $n_{sv} \sim \eta$ . In principle, CPD-SVR is able to predict a more compact expansion form than SOP-NN, namely  $n_{sv} \lesssim \eta$ , due to the follow-



ing several points. First, the single-layer NN function  $V^{(\text{SOP-NN})}$  needs lots of neurons to approach convergence leading to the rank of  $V_I^{(\text{SOP-NN})}$  might be very high for complex multi-dimension systems. It was proved<sup>20</sup> that GPR is equivalent to single-layer NN with infinite neurons and thus the single-layer NN function predict the CPD form with very large rank (*i.e.*,  $\eta \rightarrow \infty$ ) if it approaches convergence. This might greatly limit application of SOP-NN to multi-dimension systems. Obviously, it is still insufficient to obtain the conclusion of  $n_{\text{sv}} \lesssim \eta$  leading to the second point. It has been proved<sup>20,26,28,40-42</sup> that the KMR methods, such as GPR, are easier to handle benefiting from the Bayesian model allowing one to construct the PES with fewer training energy data. In this context, the rank of  $V_I^{(\text{CPD-GPR})}$  may be not too large, namely  $n \lesssim \eta$ . Further noting  $n_{\text{sv}} < n$  (see Figure 5 for example), the CPD-SVR method has capability in building a more compact expansion CPD form than the CPD-GPR method because the ratio  $n_{\text{sv}}/n$  must be not larger than 1. Therefore, one can have  $n_{\text{sv}} \lesssim \eta$ . Finally, like GPR, SVR is a hyper-parameter regression method in which the SVR prediction model itself has already been optimized<sup>20</sup> on the basis of GLR. However, as shown in Sections III A and III B, SVR is an incomplete hyper-parameter method where part of hyper-parameters are not optimized and has to be artificially chosen. This is not the case of GPR where all of hyper-parameters are optimized. This further indicates that SVR should be more accurate if the hyper-parameters are totally optimized. This is planned in our next work.

Third, similar to SOP-NN<sup>21,22</sup>, CPD-GPR<sup>25</sup>, and present CPD-ws-SVR method, the SOP/CP-FBR methods proposed by Peláez and co-workers<sup>23,24</sup> have capability to construct the SOP/CPD form employing the two-step scheme. In SOP/CP-FBR<sup>23,24</sup>, one first guesses an initial SOP/CPD form on a coarse grid. The hyper-parameters of such form are optimized while the SOP/CPD form is interpolated into a fine grid. To easily construct the initial SOP/CPD form, the SPPs are replaced by an analytical functions, called Schmidt functions<sup>23</sup>, which are expanded in a given polynomial series, such as Chebyshev polynomial series. In SOP/CP-FBR, the potential tensors on grid  $I$  are given by<sup>23,24</sup>

$$V_I^{(\text{SOP-FBR})} = \sum_{j_1=1}^{m_1} \cdots \sum_{j_f=1}^{m_f} C_{j_1, \dots, j_f} \prod_{\kappa=1}^f \left( \sum_{\mu=1}^{t_\kappa} c_{\mu, j_\kappa}^{(\kappa)} T_\mu(q_{i_\kappa}^{(\kappa)}) \right), \quad V_I^{(\text{CP-FBR})} = \sum_{r=1}^R \lambda_r \prod_{\kappa=1}^f \left( \sum_{\mu=1}^{t_\kappa} c_{\mu, r}^{(\kappa)} T_\mu(q_{i_\kappa}^{(\kappa)}) \right), \quad (18)$$

where  $c_{\mu, j_\kappa}^{(\kappa)}$  and  $c_{\mu, r}^{(\kappa)}$  are expansion coefficients while  $T_\mu(\cdot)$  is Chebyshev function. The core tensor and expansion coefficients can be then optimized to approach a given accuracy level. Equation

(18) is able to be used in any set of grids if the SPPs are interpolated through

$$v_j^{(\kappa)}(q_{i_k}^{(\kappa)}) = \sum_{\mu=1}^{t_\kappa} c_{\mu,j_k}^{(\kappa)} T_\mu(q_{i_k}^{(\kappa)}). \quad (19)$$

The denotions in Equations (18) and (19) as well as numerical details of SOP/CP-FBR can be found in References<sup>23,24</sup>. The SOP/CP-FBR methods<sup>23,24</sup> have capability to save computational cost of the subsequent quantum dynamics calculations due to the sparse character of the Tucker core tensors. Comparing Equation (18) with Equation (5), CP-FBR predicts similar functional form of CPD-SVR. This is not surprising because both CP-FBR and CPD-GPR are concerned on the CPD form. Due to its completeness, any kernel function can be expanded through a set of Chebyshev basis functions and thus the CPD-SVR/GPR methods predict equivalent CPD form of CP-FBR with  $t_\kappa \rightarrow \infty$ .

In addition to the grid-based representation, the so-called “direct” or on-the-fly dynamics methods exist. The past decade has seen a burst of activity in the development of the direct methods merging the data-driven techniques and wave function propagation schemes such as the on-the-fly version of MCTDH. In these approaches<sup>43–45</sup>, the PESs are generated in tandem with wave function propagation making accurate on-the-fly simulations on inactivated motions possible. The on-the-fly simulations circumvent the challenge of obtaining training data by instead only demanding expensive *ab initio* calculations when they are needed. To reduce the number of terms in the PES expansion for on-the-fly MCTDH, Habershon and co-workers<sup>43–45</sup> proposed an algorithms for tensor decomposition of the KMR prediction. To this end, a secondary function decomposition<sup>45</sup> has to be performed in addition to the KMR procedure. At the first step, the potential function is represented at the grids along each DOF with the remaining coordinates fixed. At the second step, couplings between each pair of DOFs are then accounted by singular value decomposition (SVD). One creates a two-dimensional grid of a pair of DOFs and then evaluates the KMR prediction at each grid. The one-dimensional terms, calculated previously in the first step, are then subtracted from these grids to give a two-dimensional residue matrix which is subjected to SVD. This decomposition procedure<sup>45</sup> can be extended to three-dimensional terms and similarly further. In such extentions, an additive kernel including terms of at least three dimensions must be used. Comparing this procedure of Habershon and co-workers<sup>43–45</sup> with the present CPD-ws-SVR approach, the present CPD-SVR approach is a one-step procedure. It is clearly different from the decomposition algorithms of Habershon and co-workers<sup>43–45</sup>, where an existed function in general analytical form should be constructed by KMR. In general, the latter two-step scheme<sup>43–45</sup> is sim-

ilar to the traditional procedure of the Heidelberg version of MCTDH<sup>9-11</sup>, as shown in Figure 1. But, Habershon's two-step procedure<sup>43-45</sup> is employed to the on-the-fly quantum dynamics instead of the wave function propagations on an existed PES.

#### IV. CONCLUSIONS

In this work, a decoupled SVR approach in conjunction with a warm-started scheme for direct canonical polyadic decomposition of a PES through a set of discrete training energy data has been proposed to avoid the PES in general form as intermediate in quantum dynamics calculations. The present CPD-ws-SVR approach requires the multi-dimension kernel function in a product of a series of one-dimension functions, similar to recently developed CPD-GPR method<sup>25</sup>. Due to the fact that only a small set of support vectors play a role in SVR prediction, the present CPD-ws-SVR approach could predict the CPD form in lower rank than CPD-GPR. It should be noted that, the warm-started scheme needs a pre-existed crude PES to save computational cost in determining support vectors. To test the present CPD-ws-SVR approach, the PES of the H + H<sub>2</sub> system is constructed in the CPD form through discrete training energy data which are computed by existed BKMP2 PES. With the the dynamics results computed by the decomposed PESs, a good agreement among those by POTFIT, MCCPD, CPD-GPR, and CPD-ws-SVR can be clearly found. Moreover, the 6D PESs in the CPD form of the H<sub>2</sub> + H<sub>2</sub> and H<sub>2</sub>/Cu(111) systems are constructed by CPD-GPR and CPD-ws-SVR methods to show the power of SVR in reducing the CPD rank. These calculations indicate that SVR is able to reduce the CPD rank by roughly 70% ~ 80% depending on the number of training data. Finally, discussions on the present CPD-ws-SVR and relationships among CPD-ws-SVR and previously reported similar methods, such as SOP-NN, CPD-GPR, SOP-FBR, and CP-FBR, have been given. It could be clear that the present CPD-ws-SVR method should be useful in building an appropriate potential function for quantum dynamics calculations, in particular for the MCTDH calculations, and be helpful to inspire ideas for developing new tools in building decomposed potential function in lower rank. Such decomposed PES might be helpful in launching dynamics calculations based on single-particle approximation (SPA).

## ONLINE CONTENT

The Supporting Information is available free of charge at <https://pubs.acs.org/XXX/XXX>. The Supporting Information file contains: (1) various construction schemes of the PES, (2) geometries and coordinates of the three examples, (3) derivations for the working equations of the ws-SVR method, and (4) numerical details of the present quantum dynamics calculations on H + H<sub>2</sub>.

## ACKNOWLEDGMENTS

The authors gratefully acknowledges financial support by National Natural Science Foundation of China (Grant No. 22273074) and Xi'an Modern Chemistry Research Institute (Grant No. 204-J-2023-0691).

## REFERENCES

- <sup>1</sup>W. H. Miller. Recent advances in quantum mechanical reactive scattering theory including comparison of recent experiments with rigorous calculations of state-to-state cross sections for the H/D + H<sub>2</sub> → H<sub>2</sub>/HD + H reactions. *Ann. Rev. Phys. Chem.* **41** (1990), 245.
- <sup>2</sup>H.-D. Meyer, U. Manthe, and L. S. Cederbaum. The multi-configuration Hartree approach. In *Numerical Grid Methods and their Application to Schrödinger's Equation* (Dordrecht, 1993), C. Cerjan, Ed., Kluwer Academic Publishers, pp. 141–152.
- <sup>3</sup>H.-D. Meyer, U. Manthe, and L. S. Cederbaum. The Multi-Configurational Time-Dependent Hartree Approach. *Chem. Phys. Lett.* **165** (1990), 73–78.
- <sup>4</sup>U. Manthe, H.-D. Meyer, and L. S. Cederbaum. Wave-Packet Dynamics within the Multiconfiguration Hartree Framework: General Aspects and application to NOCl. *J. Chem. Phys.* **97** (1992), 3199–3213.
- <sup>5</sup>M. H. Beck, A. Jäckle, G. A. Worth, and H.-D. Meyer. The multi-configuration time-dependent Hartree (MCTDH) method: A highly efficient algorithm for propagating wave packets. *Phys. Rep* **324** (2000), 1–105.
- <sup>6</sup>U. Manthe. A multilayer multiconfigurational time-dependent Hartree approach for quantum dynamics on general potential energy surfaces. *J. Chem. Phys.* **128** (2008), 164116.

- <sup>7</sup>L. J. Doriol, F. Gatti, C. Iung, and H.-D. Meyer. Computation of vibrational energy levels and eigenstates of fluoroform using the multiconfiguration time-dependent Hartree method. *J. Chem. Phys.* **129** (2008), 224109.
- <sup>8</sup>O. Vendrell and H.-D. Meyer. Multilayer multiconfiguration time-dependent Hartree method: Implementation and applications to a Henon-Heiles Hamiltonian and to pyrazine. *J. Chem. Phys.* **134** (2011), 044135.
- <sup>9</sup>A. Jäckle and H.-D. Meyer. Reactive scattering using the multiconfiguration time-dependent Hartree approximation: General aspects and application to the collinear  $\text{H} + \text{H}_2 \rightarrow \text{H}_2 + \text{H}$  reaction. *J. Chem. Phys.* **102** (1995), 5605.
- <sup>10</sup>A. Jäckle and H.-D. Meyer. Product representation of potential energy surfaces. *J. Chem. Phys.* **104** (1996), 7974.
- <sup>11</sup>A. Jäckle and H.-D. Meyer. Product representation of potential energy surfaces II. *J. Chem. Phys.* **109** (1998), 3772.
- <sup>12</sup>D. Peláez and H.-D. Meyer. The multigrid POTFIT (MGPF) method: Grid representations of potentials for quantum dynamics of large systems. *J. Chem. Phys.* **138** (2013), 014108.
- <sup>13</sup>D. Peláez, K. Sadri, and H.-D. Meyer. Full-dimensional MCTDH/MGPF study of the ground and lowest lying vibrational states of the bihydroxide  $\text{H}_3\text{O}_2^-$  complex. *Spectrochimica Acta part A* **119** (2014), 42–51.
- <sup>14</sup>F. Otto. Multi-Layer Potfit: An accurate potential representation for efficient high-dimensional quantum dynamics. *J. Chem. Phys.* **140** (2014), 014106.
- <sup>15</sup>F. Otto, Y.-C. Chiang, and D. Peláez. Accuracy of Potfit-based potential representations and its impact on the performance of (ML-)MCTDH. *Chem. Phys.* **509** (2018), 116.
- <sup>16</sup>M. Schröder and H.-D. Meyer. Transforming high-dimensional potential energy surfaces into sum-of-products form using Monte Carlo methods. *J. Chem. Phys.* **147** (2017), 064105.
- <sup>17</sup>M. Schröder. Transforming high-dimensional potential energy surfaces into a canonical polyadic decomposition using Monte Carlo methods. *J. Chem. Phys.* **152** (2020), 024108.
- <sup>18</sup>Q. Meng, M. Schröder, and H.-D. Meyer. High-Dimensional Quantum Dynamics Study on Excitation-Specific Surface Scattering Including Lattice Effects of a Five-Atom Surface Cell. *J. Chem. Theory Comput.* **17** (2021), 2702–2713.
- <sup>19</sup>L. Shi, M. Schröder, H.-D. Meyer, D. Peláez, A. M. Wodtke, K. Golibrzuch, A.-M. Schönemann, A. Kandratsenka, and F. Gatti. Quantum and classical molecular dynamics for H atom scattering from graphene. *J. Chem. Phys.* **159** 159 (2023), 194102.

- <sup>20</sup>Q. Song, X. Zhang, Z. Miao, Q. Zhang, and Q. Meng. Unified Regression Models in Fitting Potential Energy Surfaces for Quantum Dynamics. *J. Math. Chem.* **60** (2022), 1983–2012.
- <sup>21</sup>S. Manzhos and T. Carrington, Jr. Using neural networks to represent potential surfaces as sum of products. *J. Chem. Phys.* **125** (2006), 194105.
- <sup>22</sup>W. Koch and D. H. Zhang. Separable potential energy surfaces from multiplicative artificial neural networks. *J. Chem. Phys.* **141** (2014), 021101.
- <sup>23</sup>R. L. Panadés-Barrueta and D. Peláez. Low-rank sum-of-products finite-basis-representation (SOP-FBR) of potential energy surfaces. *J. Chem. Phys.* **153** (2020), 234110.
- <sup>24</sup>N. Nadoveza, R. L. Panadés-Barrueta, L. Shi, F. Gatti, and D. Peláez. Analytical high-dimensional operators in Canonical Polyadic Finite Basis Representation (CP-FBR). *J. Chem. Phys.* **158** (2023), 114109.
- <sup>25</sup>Q. Song, X. Zhang, D. Peláez, and Q. Meng. Direct Canonical-Polyadic-Decomposition of the Potential Energy Surface from Discrete Data by Decoupled Gaussian Process Regression. *J. Phys. Chem. Lett.* **13** (2022), 11128–11135.
- <sup>26</sup>Q. Song, Q. Zhang, and Q. Meng. Revisiting the Gaussian process regression for fitting high-dimensional potential energy surface and its application to the  $\text{OH} + \text{HO}_2 \rightarrow \text{O}_2 + \text{H}_2\text{O}$  reaction. *J. Chem. Phys.* **152** (2020), 134309.
- <sup>27</sup>Q. Song, X. Zhang, Z. Miao, and Q. Meng. Construction of Mode-Combination Hamiltonian under the GridBased Representation for the Quantum Dynamics of  $\text{OH} + \text{HO}_2 \rightarrow \text{O}_2 + \text{H}_2\text{O}$ . *J. Chem. Theory Comput.* **20** (2024), 597–613.
- <sup>28</sup>Q. Song, Q. Zhang, and Q. Meng. Neural-network potential energy surface with small database and high precision: A benchmark of the  $\text{H} + \text{H}_2$  system. *J. Chem. Phys.* **151** (2019), 114302.
- <sup>29</sup>G. A. Worth, M. H. Beck, A. Jäckle, O. Vendrell, and H.-D. Meyer. The MCTDH Package, Version 8.2, (2000). H.-D. Meyer, Version 8.3 (2002), Version 8.4 (2007). O. Vendrell and H.-D. Meyer Version 8.5 (2013). Version 8.5 contains the ML-MCTDH algorithm. Current versions: 8.4.18 and 8.5.11 (2019). See <http://mctdh.uni-hd.de/>.
- <sup>30</sup>A. I. Boothroyd, P. G. Martin, W. J. Keogh, and M. J. Peterson. An accurate analytic  $\text{H}_4$  potential energy surface. *J. Chem. Phys.* **116** (2002), 666.
- <sup>31</sup>C. Díaz, R. A. Olsen, D. J. Auerbach, and G.-J. Kroes. Six-dimensional dynamics study of reactive and non reactive scattering of  $\text{H}_2$  from  $\text{Cu}(111)$  using a chemically accurate potential energy surface. *Phys. Chem. Chem. Phys.* **12** (2010), 6499.
- <sup>32</sup>P. S. Thomas, M. F. Somers, A. W. Hoekstra, and G. J. Kroes. Chebyshev high-dimensional

- model representation (Chebyshev-HDMR) potentials: application to reactive scattering of H<sub>2</sub> from Pt(111) and Cu(111) surfaces. *Phys. Chem. Chem. Phys.* **14** (2012), 8628–8643.
- <sup>33</sup>J. M. Bowman, G. Czako, and B. Fu. High-dimensional ab initio potential energy surfaces for reaction dynamics calculations. *Phys. Chem. Chem. Phys.* **13** (2011), 8094–8111.
- <sup>34</sup>J. Li, Y. Wang, B. Jiang, J. Ma, R. Dawes, D. Xie, J. M. Bowman, and H. Guo. A chemically accurate global potential energy surface for the HO + CO → H + CO<sub>2</sub> reaction. *J. Chem. Phys.* **136**, 4 (2012), 041103.
- <sup>35</sup>B. Jiang and H. Guo. Permutation invariant polynomial neural network approach to fitting potential energy surfaces. *J. Chem. Phys.* **139** (2013), 054112.
- <sup>36</sup>J. Li, B. Jiang, and H. Guo. Permutation invariant polynomial neural network approach to fitting potential energy surfaces. II. Four-atom systems. *J. Chem. Phys.* **139** (2013), 204103.
- <sup>37</sup>J. Behler. Constructing high-dimensional neural network potentials: A tutorial review. *Int. J. Quant. Chem.* **115** (2015), 1032–1050.
- <sup>38</sup>Q. Meng, J. Chen, and D. H. Zhang. Rate coefficients of the H + CH<sub>4</sub> → H<sub>2</sub> + CH<sub>3</sub> reaction from ring polymer molecular dynamics on a highly accurate potential energy surface. *J. Chem. Phys.* **143** (2015), 101102.
- <sup>39</sup>Z. Miao, X. Zhang, Y. Zhang, L. Wang, and Q. Meng. Chemistry-Informed Generative Model for Classical Dynamics Simulations. *J. Phys. Chem. Lett.* **15** (2024), 532–539.
- <sup>40</sup>A. Kamath, R. A. Vargas-Hernández, R. V. Krems, T. Carrington, and S. Manzhos. Neural networks vs Gaussian process regression for representing potential energy surfaces: A comparative study of fit quality and vibrational spectrum accuracy. *J. Chem. Phys.* **148** (2018), 241702.
- <sup>41</sup>R. V. Krems. Bayesian machine learning for quantum molecular dynamics. *Phys. Chem. Chem. Phys.* **21** (2019), 13392–13410.
- <sup>42</sup>R. A. Vargas-Hernández, Y. Guan, D. H. Zhang, and R. V. Krems. Bayesian optimization for the inverse scattering problem in quantum reaction dynamics. *New J. Phys.* **21** (2019), 022001.
- <sup>43</sup>G. W. Richings and S. Habershon. Direct Quantum Dynamics Using Grid-Based Wave Function Propagation and Machine-Learned Potential Energy Surfaces. *J. Chem. Theory Comput.* **13** (2017), 4012–4024.
- <sup>44</sup>G. W. Richings and S. Habershon. MCTDH on-the-fly: Efficient grid-based quantum dynamics without pre-computed potential energy surfaces. *J. Chem. Phys.* **148** (2018), 134116.
- <sup>45</sup>G. W. Richings and S. Habershon. Predicting Molecular Photochemistry Using Machine-Learning-Enhanced Quantum Dynamics Simulations. *Acc. Chem. Res.* **55** (2022), 209–220.

TABLE I: Updating scheme of the present warm-started algorithm for building the PES by SVR. The working equations of this scheme are given by Equations (14) and (15). In general, the present implementation requires various updating cases for the training points as well as error function and parameters. According to the new points added into the model, two updating cases exist. It is a simple and easy case if a new point is added into  $\mathcal{R}$  because nothing needs to be changed. The other case has four updating situations of error function and parameters, according to the updating possibilities of the training points. Illustrated in Figure 3 are diagrammatic sketch for updating the points. The second column gives items to estimate the updating cases. These evaluation items are (1) the set into which the new point is added, (2) illustration of the updating scheme, (3) change of error function. The updating of points and functions are also given. The other columns give the updating processes for Cases #1 and #2. The rightmost four columns give four situations of Case #2.

No.	Item	Case #1		Case #2			
		Case #2.1	Case #2.2	Case #2.3	Case #2.4		
1	Adding point	Into $\mathcal{R}$					
2	Illustration	Upper panel of Figure 3		Lower panel of Figure 3			
3	Consequence	$ h(\mathbf{X}_\ell)  < \epsilon$		$ h(\mathbf{X}_\ell)  \geq \epsilon$			
4	Updating points	Unchange the other points	$\mathcal{E} \rightarrow \mathcal{S}$	$\mathcal{R} \rightarrow \mathcal{S}$	$\mathcal{S} \rightarrow \mathcal{R}$	$\mathcal{S} \rightarrow \mathcal{E}$	
5	Updating $h(\mathbf{X}_i)$	–	$\Delta h(\mathbf{X}_{e_i}) = \pm\epsilon - h(\mathbf{X}_{e_i})$	$\Delta h(\mathbf{X}_{r_i}) = \pm\epsilon - h(\mathbf{X}_{r_i})$	–	–	–
6	Updating $\varphi_\ell$	–	$\Delta\varphi_\ell = \gamma_{e_i}^{-1}(\pm\epsilon - h(\mathbf{X}_{e_i}))$	$\Delta\varphi_\ell = \gamma_{r_i}^{-1}(\pm\epsilon - h(\mathbf{X}_{r_i}))$	$\Delta\varphi_\ell = \lambda_{s_i}^{-1}\varphi_{s_i}$	$\Delta\varphi_\ell = \lambda_{s_i}^{-1}(\pm c - \varphi_{s_i})$	



TABLE II: Three typical examples for testing the present CPD-ws-SVR calculations together with numerical details for SVR. The second column gives items for estimating the calculations. These items contain (1) dimensionality, (2) geometry, (3) coordinates set, (4) tolerance and validate errors, (5) number of training data  $n$  for final SVR calculations. Number of supporting vectors  $n_{sv}$  and ratio  $n_{sv}/n$  depend on  $n$  implying that  $n_{sv}$  has no determine value. Definitions and geometries of these systems are also given in the Supporting Information file. The third, fourth, and fifth columns give details of  $H + H_2$ ,  $H_2 + H_2$ , and  $H_2/Cu(111)$ , respectively.

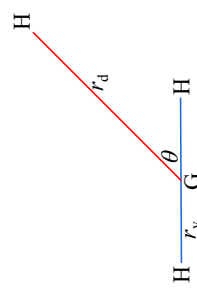
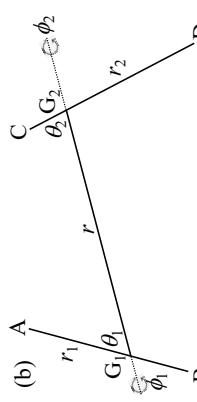
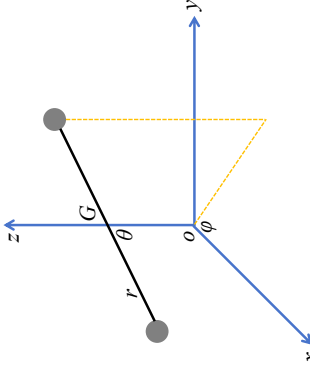
No.	Item	Systems		
1	Dimensionality	$H + H_2$	$H_2 + H_2$	$H_2/Cu(111)$
2	Geometry			
3	Coordinates	$\{r_d, r_v, \theta\}$	$\{r, r_1, r_2, \theta_1, \theta_2, \phi = \phi_1 - \phi_2\}$	$\{x, y, z, r, \theta, \phi\}$
4	Tolerance error	$10^{-4}$	$10^{-4}$	$10^{-4}$
5	Validate error	$\sim 10^{-3}$	$\sim 10^{-2}$	$\sim 10^{-2}$
6	$n$	$9.0 \times 10^3$	$9.5 \times 10^4$	$9.5 \times 10^4$

TABLE III: DVR-grids of the wave function representation and parameters of the initial condition for the present MCTDH calculations. The definitions of the coordinates (indicated in the first column) are given in Table II. The second column describes the primitive basis functions, which underlay the DVR basis. The third column gives the number of the grid points. The fourth column gives the range of the grids in bohr or radian. The fifth column gives the symbol of the one-dimensional (1D) function for each coordinate of the initial wave function in relaxations for the ro-vibrational eigen-states. The other columns give the parameters for these 1D functions, including positions and momenta in the 1D function, width of the Gaussian function (*i.e.*, variance of the modulus-square of the Gaussian function,  $W_{\text{GAUSS}}$ ), and the initial quantum number  $j_{\text{ini}}$  of the angular function.

Coordinates	Primitive basis function			Initial wave function			
	Symbol <sup>a</sup>	Grid points	Range of the grids	Symbol <sup>b</sup>	Position	Momentum	Parameters
$r_d$	SIN	68	[1.00, 9.04]	GAUSS	4.50	-8.00	$W_{\text{GAUSS}} = 0.25$ Bohr
$r_v$	SIN	48	[0.60, 6.24]	EIGENF	-	-	ground state
$\theta$	LEG	31	$[0, \pi]$	LEG	-	-	$j_{\text{ini}} = 0$ , sym

<sup>a</sup> Symbol ‘‘SIN’’ stands for sine DVR. Symbol ‘‘LEG’’ denotes one-dimensional Legendre DVR for angular coordinate.

<sup>b</sup> Symbol ‘‘GAUSS’’ designates the choice of Gaussian function as initial SPFs. Symbol ‘‘EIGENF’’ means eigenfunction of a specified potential which, in this work, is reduced one-dimensional potential function of  $\text{H}_2$  calculated from the PES. Symbol ‘‘LEG’’ denotes Legendre function to specify the initial wave function.

## FIGURE CAPTIONS

**Figure 1:** Construction schemes of the potential function in the CPD form where the training data have already been computed by *ab initio*. This special expansion tensor form is useful and helpful to resolving high-dimension working equations of quantum dynamics. The black boxes give computational inputs and outputs. The red boxes give computational techniques. Here, the regression methods contain those of either NN or GPR, while the re-fitting methods mean POTFIT, MGPF, MLPF, MCPF, or MCCPD. The clockwise pathway represents the traditional scheme reproducing the PES in an arbitrary form. In general, this form can be used for both classical and quantum dynamics calculations. For special cases, such as the ML-MCTDH calculations, the PES has to be re-fitted in either SOP or CPD form. The anticlockwise pathway represents the direct scheme proposed by the previous CPD-GPR and the present CPD-SVR approaches. This scheme directly reproduces the PES in the CPD form through either GPR or SVR. Therefore, the traditional and direct schemes have two and one regression steps, respectively. Since numerical regressions reproduce errors in either traditional or direct scheme, the direct scheme with only one step is much more efficient and accurate than the traditional one.

**Figure 2:** Schematic illustrations on (a) the core ideas of SVR and support vector and (b) the dependence of the tolerance error and the fitting error, where the abscissa and ordinate axes represent the coordinate  $\mathbf{x}$  and electronic energy  $V$ , respectively. The gray line represents the target PES denoted by  $0$ , while the red and blue lines are parallel to the prediction and denoted by  $\pm\epsilon$ . In SVR, only the points outside the region surrounded by red and blue lines contribute to the cost insofar. It turns out that in most cases the optimization problem can be solved more easily in its dual formulation. The support vectors in SVR are the data that lie on and outside the two hypersurfaces (represented by blue and red lines) that are parallel to the target hypersurface, namely the SVR prediction (represented by gray line) with distances of tolerance error  $\pm\epsilon$ . The support vectors are points most difficult to regress such that they have direct bearing on the optimum location of the target prediction function. The optimal PES (the gray line) stems from the function class with the biggest “capacity” of independent samples that one can twiddle keeping the functional form not too complex. Furthermore, in subfigure (b) the solid and dashed lines represent the hypersurfaces for  $\epsilon$  and  $\epsilon'$ , respectively, while the blue and red lines are those associated with those with different symbols. The optimal potential function (the gray line) stems from the function class with the

biggest capacity of independent samples that one can twiddle keeping the functional form not too complex. Therefore, in principle, the fitting error depends on the tolerance error. If only few of noises exist in the training database the support vectors should independent on the choice of tolerance error.

**Figure 3:** Updating scheme of the classifications of the training points when a new point is added into the optimization procedure. The core idea of SVR and support vector is given in the main text. When a new training point is added, the decision hypersurface should be updated so that all of previously optimized results should be updated according to the present ws-SVR approach. The upper and lower panels illustrate two cases for adding new training points. Given in the upper panel is Case #1, where the new training point is added into  $\mathcal{R}$  implying that  $|h| < \epsilon$  and the other points are unchanged. The lower panel illustrates Case #2, where the new training point is added into  $\mathcal{E}$  or  $\mathcal{S}$ . In Case #2 the decision surface of the last round has to be changed and hence the classifications are changed. To keep the training points belonging to their original sets as much as possible, one can find four different situations in changing the classification during optimization. In these subfigures, the red, blue, and yellow black circles represent the training points belonging to  $\mathcal{S}$ ,  $\mathcal{R}$ , and  $\mathcal{E}$ , respectively, while the black point represents the newly adding point.

**Figure 4:** Validation errors (RMSE values in hartree) of the present CPD-ws-SVR calculations as functions of number of training data  $n$  for the  $\text{H} + \text{H}_2$  system. These SVR calculations are performed using various tolerance errors. The red, blue, and black lines and symbols represent errors computed with tolerance errors of  $10^{-2}$ ,  $10^{-3}$ , and  $10^{-4}$  hartree, respectively. All of training data are computed through pre-existed BKMP2 potential function where they are randomly sampled in the whole configurational space. The error bars are obtained through 5-fold cross validation (5-CV), where the validation set comprises of 20% of the whole database.

**Figure 5:** Numbers of training data  $n$  and support vectors  $n_{sv}$  together with ratios  $n_{sv}/n$  for various potential energy intervals of the  $\text{H} + \text{H}_2$ . In fitting this PES, the tolerance error is  $10^{-4}$  hartree. The abscissa axis gives seven uniform intervals for the potential energy less than zero. Each interval represents an energy range of about 0.62 eV. The left axis represents numbers of data while the right axis represents the ratio  $n_{sv}/n$ . The red and blue columns give numbers of support vectors and

training data, respectively. The black dots represent the ratios  $n_{sv}/n$  in percentage. The support vectors in SVR are the data that lie on and outside the two hypersurfaces that are parallel to the target hypersurface. Thus, the support vectors are points most difficult to regress such that they have direct bearing on the optimum location of the target prediction function. In this context, ratios  $n_{sv}/n$  must be smaller than one.

**Figure 6:** The contour cuts of the SVR potential tensor on the  $r_d$ - $r_v$  plane with  $\theta = \pi/2$  for the  $H + H_2$  system. The definitions of coordinates  $r_v$ ,  $r_d$ , and  $\theta$  are given in Table II. Here, we set the potential energy of the totally separated three H atoms to be zero. To draw this potential tensor, the grids of the  $r_d$ - $r_v$  plane are set to be  $68 \times 48$  equal to those given in Table III. Moreover, the 3D graphics of the potential function  $V(r_d, r_v, \theta = \pi/2)$  is also given, where the coordinate variables  $r_d$  and  $r_v$  are given in bohr while the potential energy is given in eV.

**Figure 7:** Energy-dependent reactive probabilities versus total energy (in eV) for the  $H' + H_2 \rightarrow HH' + H$  reaction where the PES is transferred into various tensor forms in performing the quantum dynamics calculations. The green, blue, red, and black lines represent the reactive probabilities computed on the basis of the *potfitted*, *mccpded*, CPD-GPR, and CPD-ws-SVR potential tensors. The *potfitted* and *mccpded* potential tensors are constructed by POTFIT and MCCPD through the BKMP2 PES, respectively. Numerical details of these calculations were reported in Reference<sup>25</sup>. The CPD-GPR and CPD-ws-SVR tensors are constructed on the basis of the same training sets with  $n = 9000$ , where the CPD-GPR calculation was already reported in Reference<sup>25</sup>. Error convergence of the CPD-ws-SVR calculation is illustrated in Figure 4.

**Figure 8:** Validation errors (RMSE values in hartree) of (a) the present CPD-GPR calculations and (b) the present 6D CDP-ws-SVR calculations as functions of number of training data  $n$  for  $H + H_2$ ,  $H_2 + H_2$ , and  $H_2/Cu(111)$ . The blue and red lines represent errors computed for the  $H_2 + H_2$  and  $H_2/Cu(111)$  systems, respectively, while the green line in subfigure (a) gives errors for  $H + H_2$ . The similar CPD-ws-SVR error curves for  $H + H_2$  are illustrated in Figure 4. The errors are obtained by averaging five-times calculations at the same setup, where the validation set comprises of 20% of the whole database. All of data, in either training set or validation set, are randomly

sampled in the configurational space.

**Figure 9:** The ratios  $n_{sv}/n$  as function of the number of training data  $n$  for the  $H_2 + H_2$  and  $H_2/Cu(111)$  systems, given by the blue and red lines, respectively, where  $n_{sv}$  is the number of support vectors. The same curve for the  $H + H_2$  system has been illustrated by the black dots of Figure 5. The abscissa and ordinate axes represent number of training data  $n$  and ratios  $n_{sv}/n$ , respectively. For simple, the abscissa axis is given by logarithmic scale instead of linear scale.

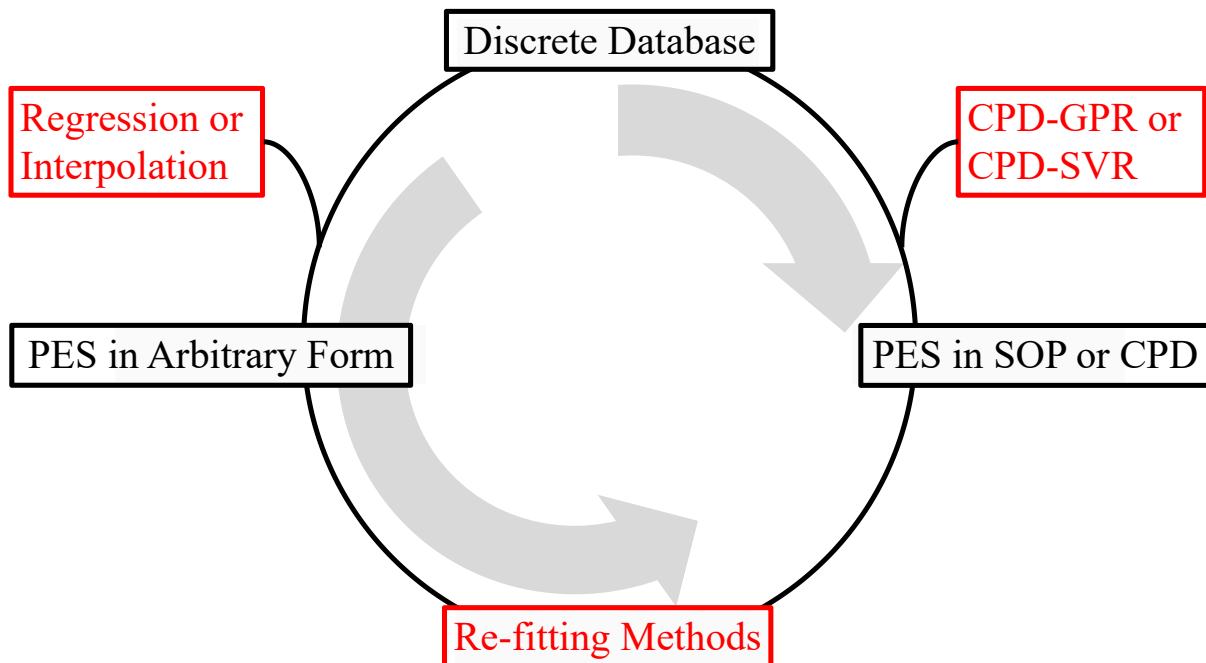
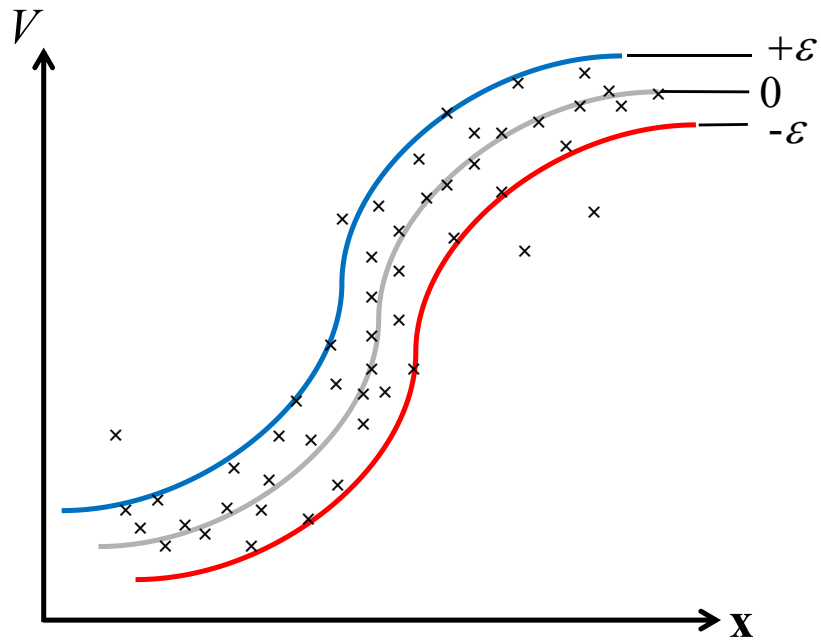
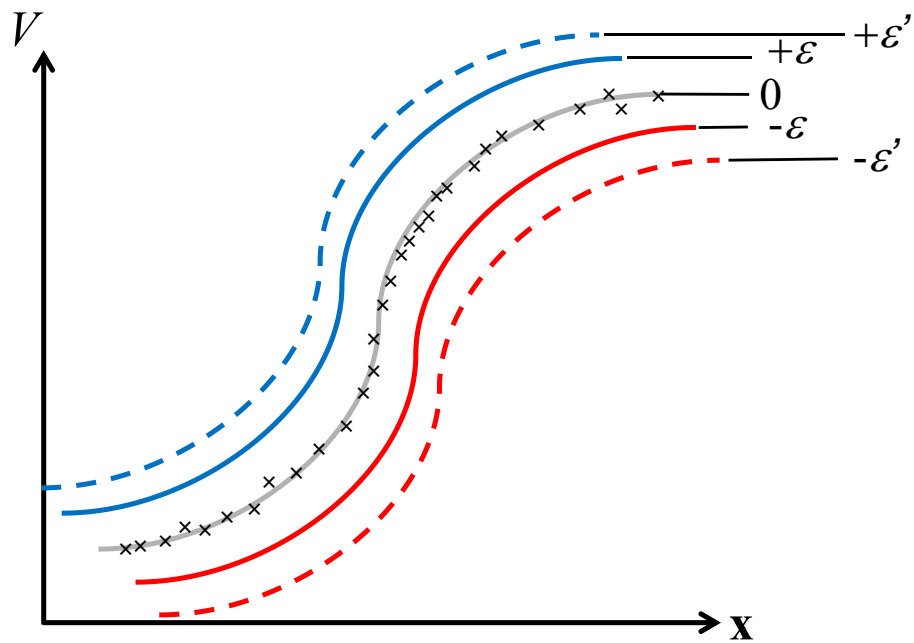


FIG. 1: CPD-SVR, Meng



(a) Core ideas of SVR and support vector



(b) Dependence of tolerance and error

FIG. 2: CPD-SVR, Meng



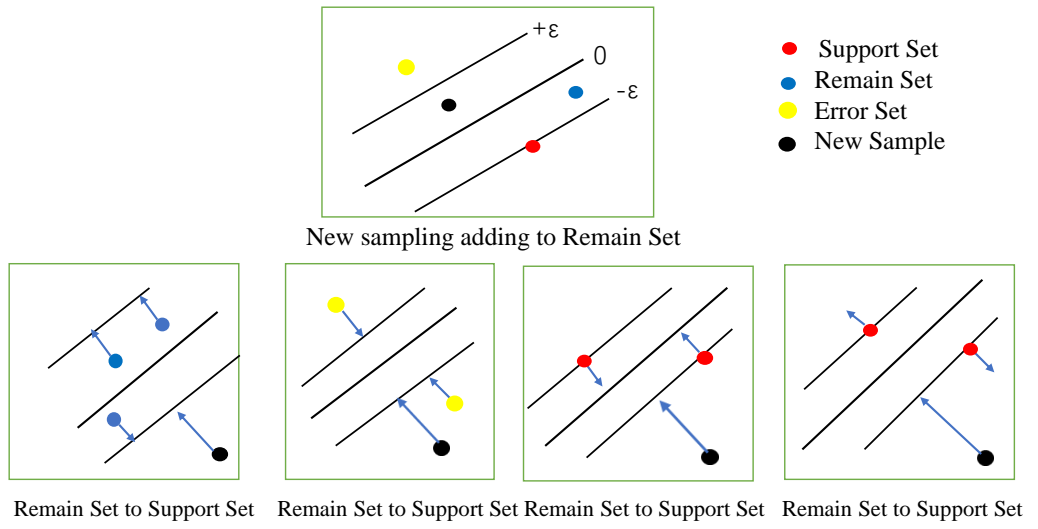


FIG. 3: CPD-SVR, Meng

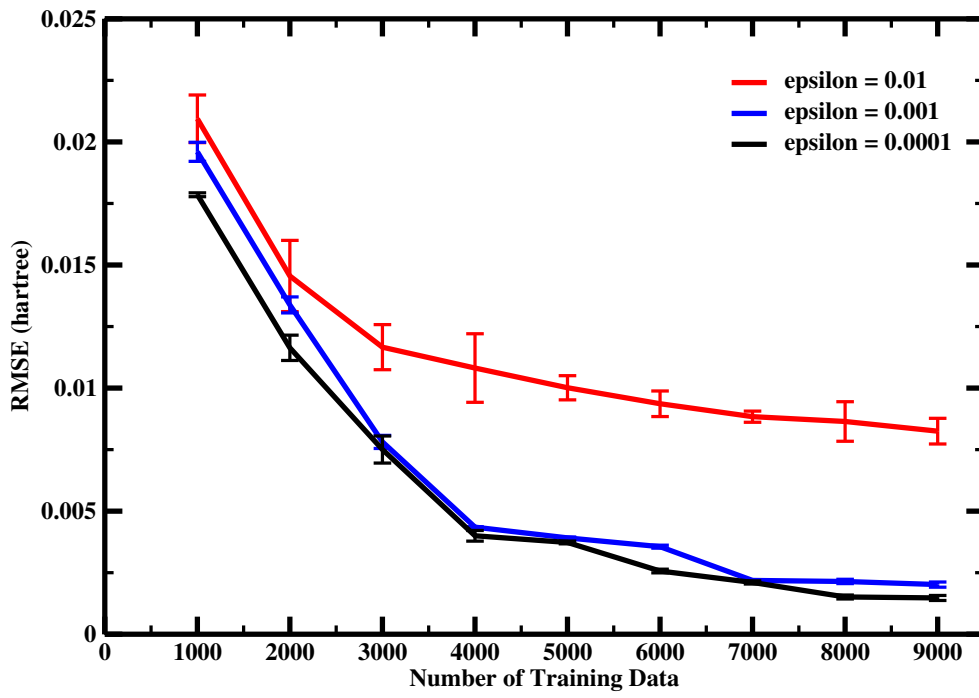


FIG. 4: CPD-SVR, Meng

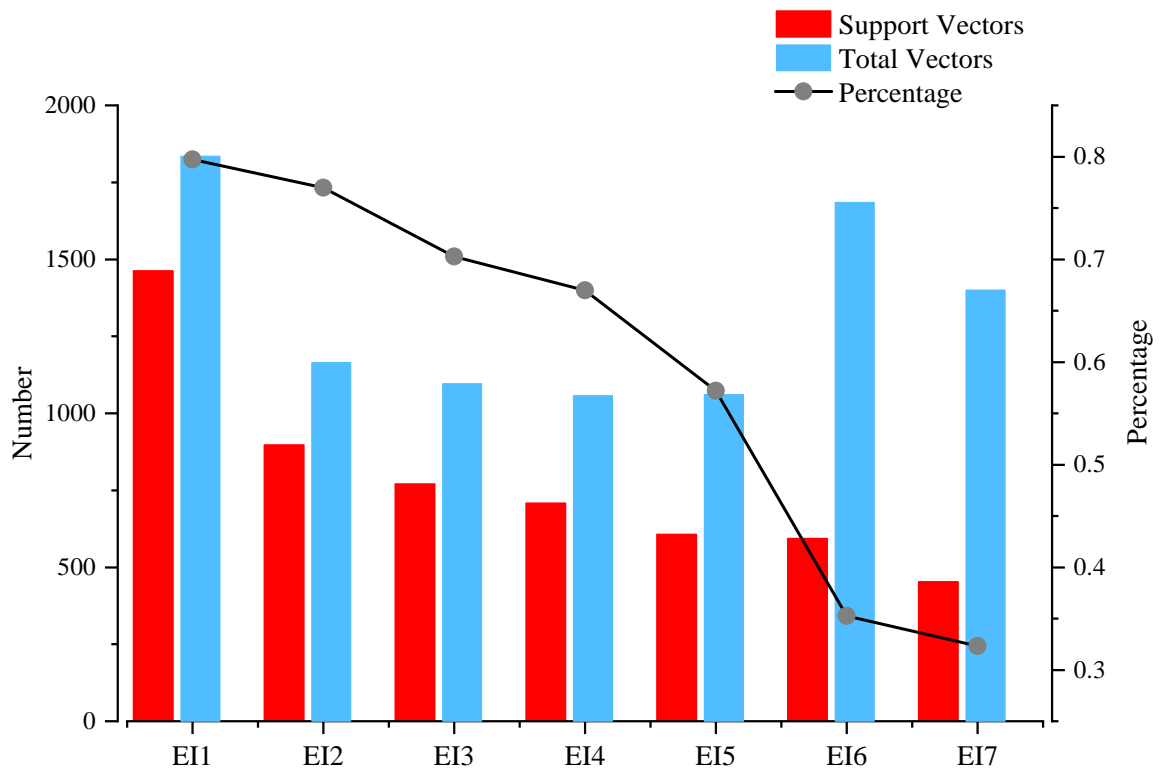


FIG. 5: CPD-SVR, Meng

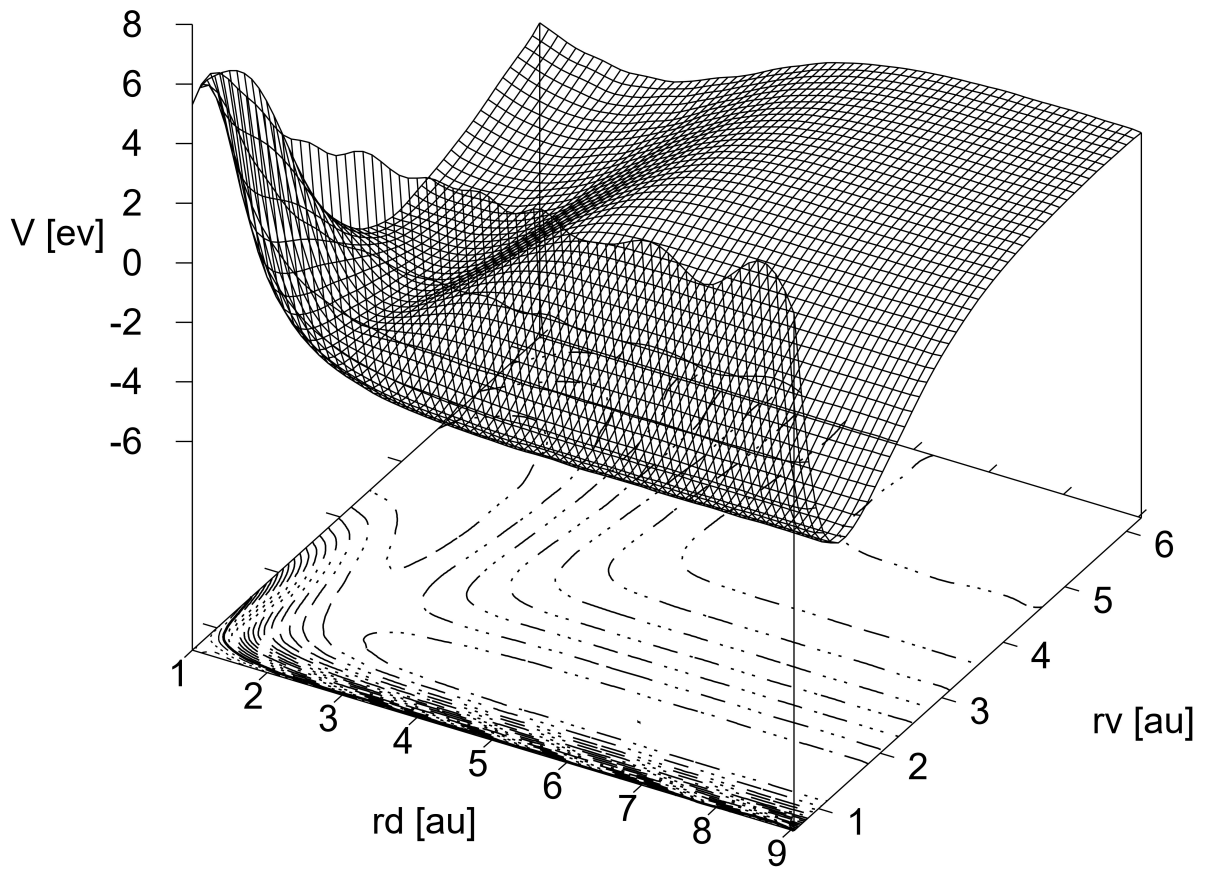


FIG. 6: CPD-SVR, Meng

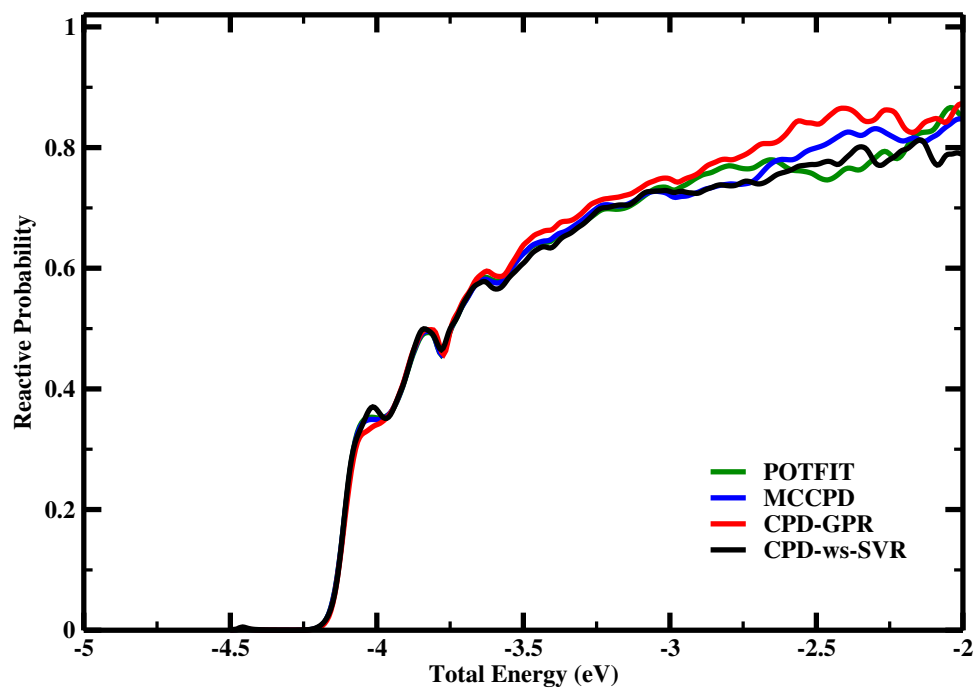
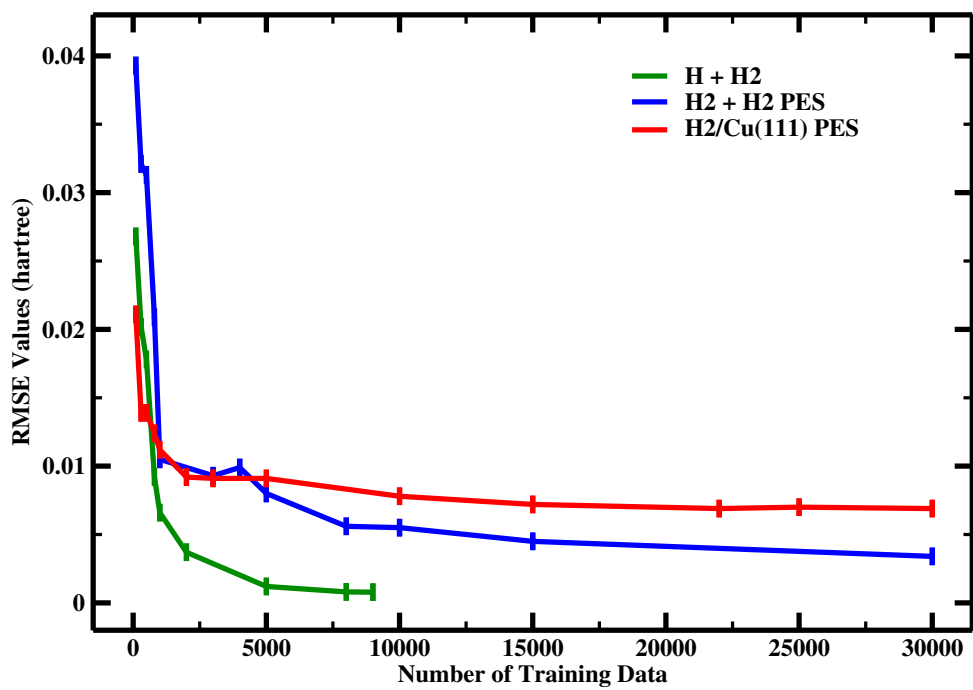
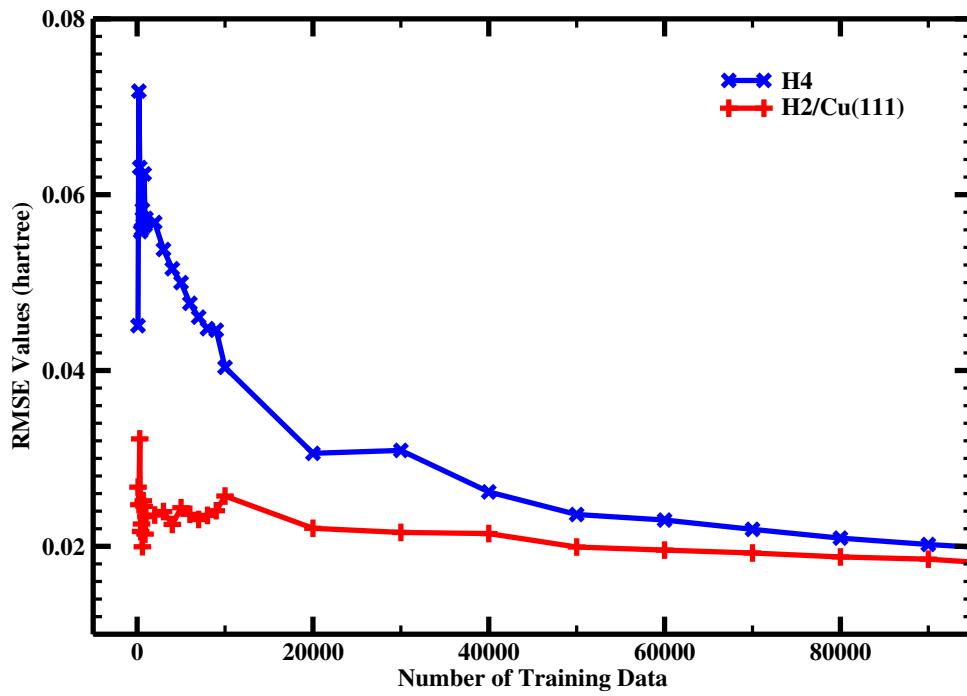


FIG. 7: CPD-SVR, Meng



(a) Convergence inspection of the CPD-GPR calculations



(b) Convergence inspection of the CPD-ws-SVR calculations

FIG. 8: CPD-SVR, Meng

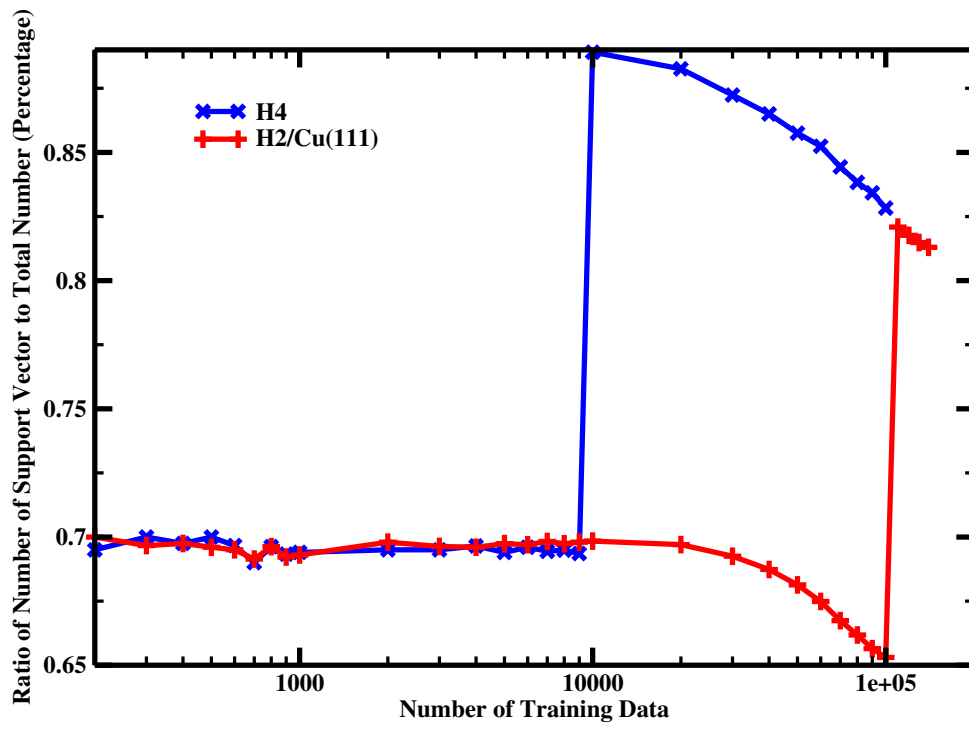


FIG. 9: CPD-SVR, Meng